# Developmental control of plant Rho GTPase nano-organization by the lipid phosphatidylserine

Matthieu Pierre Platre, Vincent Bayle, Laia Armengot, Joseph Bareille, Maria del Mar Marquès-Bueno, Audrey Creff, Lilly Maneta-Peyret, Jean-Bernard Fiche, Marcelo Nollmann, Christine Miege, et al.

Title: **Developmental control of plant Rho GTPase nano-organization by the lipid phosphatidylserine**

**Authors:** Matthieu Pierre Platre[1], Vincent Bayle[1], Laia Armengot[1], Joseph Bareille[1], Maria Mar Marques-Bueno[1], Audrey Creff[1], Lilly Maneta-Peyret[2], Jean-Bernard Fiche[3], Marcelo Nolmann[3], Christine Miège[1], Patrick Moreau[2,4], Alexandre Martinière[5] and Yvon Jaillais[1*]

**Affiliations:**

[1]Laboratoire Reproduction et Développement des Plantes, Université de Lyon, ENS de Lyon, UCB Lyon 1, CNRS, INRA, F-69342 Lyon, France.

[2]UMR 5200 Membrane Biogenesis Laboratory, CNRS-University of Bordeaux, Bâtiment A3 - INRA Bordeaux Aquitaine, 71 Avenue Edouard Bourlaux- CS 20032, 33140 Villenave d'Ornon, France.

[3]Centre de Biochimie Structurale, CNRS UMR5048, INSERM U1054, Université de Montpellier, 29 Rue de Navacelles, 34090, Montpellier, France.

[4]Bordeaux Imaging Center, UMS 3420 CNRS, US4 INSERM, University of Bordeaux, 33000 Bordeaux, France.

[5]BPMP, Univ Montpellier, CNRS, INRA, Montpellier SupAgro, Montpellier, France.

*Correspondence to: yvon.jaillais@ens-lyon.fr

**Changes made during the revisions are highlighted in green**

**Abstract:**

Rho GTPases are master regulators of cell signaling, but how they are regulated depending on the cellular context is unclear. Here, we show that the phospholipid phosphatidylserine acts as a developmentally-controlled lipid rheostat that tunes Rho GTPase signaling in Arabidopsis. Live super-resolution single molecule imaging revealed that RHO-OF-PLANT6 (ROP6) is stabilized by phosphatidylserine into plasma membrane nanodomains, which is required for auxin signaling. Furthermore, we uncovered that the plasma membrane phosphatidylserine content varies during plant root development and that the level of phosphatidylserine modulates the quantity of ROP6 nanoclusters induced by auxin and hence downstream signaling, including regulation of endocytosis and gravitropism. Our work reveals that variations in phosphatidylserine levels are a physiological process that may be leveraged to regulate small GTPase signaling during development.

**One Sentence Summary:**

Phosphatidylserine acts as a developmentally-controlled lipid rheostat that regulates auxin sensitivity and plant development.

**Main Text:**

Proteins from the Rho/Ras superfamily are small GTPases that regulate fundamental eukaryotic functions, including cell signaling, cell polarity, intracellular trafficking and cytoskeleton dynamics (*1, 2*). Furthermore, they control the morphology and behavior of cells and organisms by integrating signaling pathways at the cell surface into various cellular outputs. The small GTPase paradigm stipulates that they are in an "inactive" form when bound to GDP, and in an "active" form when bound to GTP. However, emerging evidence suggest that this view is likely oversimplified, since their membrane environment also dictates the signaling capacity of these GTPases (*2*). For example, Ras/Rho signaling is intimately linked with membrane lipids in all eukaryotes. Interaction with anionic lipids is important for their plasma membrane targeting (*3, 4*), but also mediates the clustering of these small GTPases at the cell surface into nanometer scale membrane domains (*5-8*). In particular, the phospholipid phosphatidylserine is involved in the nanoclustering and signaling of some GTPase, such as K-Ras in human and Cdc42 in yeast (*2, 7, 8*). By contrast to other anionic phospholipids, phosphatidylserine is relatively abundant, representing up to 10-20% of the total phospholipids at the plasma membrane inner leaflet (*9*). In addition, phosphatidylserine is not constantly modified by specialized metabolizing enzymes and its subcellular repartition is thought to be relatively stable across cell types (*9, 10*). Therefore, phosphatidylserine appears to be a structural component of the membrane, which is required for K-Ras/Cdc42 nanoclustering. It is unknown, however, whether phosphatidylserine also has a regulatory role in vivo in modulating nanocluster formation and subsequent signaling. In other words, is phosphatidylserine function in GTPase nanoclustering rate limiting? And if yes, are phosphatidylserine levels regulated during development and what are the consequences of such changes on small GTPases signaling capacity? Here, we addressed these questions using the *Arabidopsis thaliana* root as a model system, because it is a genetically tractable multicellular organ, with a variety of cell types and cell differentiation states and amenable to live imaging.

In plants, there is a single protein family in the Ras/Rho GTPase superclade, called ROP for RHO-OF-PLANT(*11*). ROPs are master regulators of cell polarity and cell morphogenesis, but they also sit at the nexus of plant hormone signaling (including auxin and abscisic acid), cell wall sensing pathways and receptor-like kinase signaling (involved in development, reproduction and immunity) (*11-18*). Here, we show that auxin triggers ROP6 nanoclustering within minutes, in a phosphatidylserine dependent manner. Furthermore, we found that phosphatidylserine is required for ROP6 signaling, and variations in the cellular phosphatidylserine content directly impact the quantity of ROP6 nanoclusters and thereby subsequent downstream auxin signaling, including the regulation of endocytosis and root gravitropism. Therefore, phosphatidylserine is not a mere structural component of the membrane, it is a *bona fide* signaling lipid that acts as a developmentally-controlled lipid rheostat to regulate small GTPases in a cell-context dependent manner.

## Results and discussion

### Phosphatidylserine localization varies during root cell differentiation.

Phosphatidylserine is an anionic phospholipid that partitions between the cytosolic leaflets of the plasma membrane and endosomes (*10*). Bulk phosphatidylserine measurements in *Arabidopsis thaliana* suggested that the relative phosphatidylserine concentration can vary in vivo depending on the organ (*19*). In order to get tissue and cellular resolution on the phosphatidylserine

distribution, we recently validated the use of two phosphatidylserine reporters in *Arabidopsis*, the C2 domain of Lactadherin ($C2_{Lact}$) and the PH domain of EVECTIN2 ($2xPH_{EVCT2}$) (*10*, *20*). In both cases, the proportion of phosphatidylserine sensors was markedly more pronounced at the plasma membrane than endosomes in the root basal meristem compared to cells in the elongation zone (Fig. 1A, Fig. S1). This developmental gradient appeared to be in part regulated by the plant hormone auxin, as relatively short treatment (60min) with the synthetic auxin naphthalene-1-acetic acid (NAA) increased the level of both phosphatidylserine sensors at the plasma membrane at the expense of their endosomal localization in the elongation zone (Fig. 1B, Fig. S1C). Therefore, not only the overall phosphatidylserine level varies depending on the organ but there are also local variations of the phosphatidylserine content at the plasma membrane within an organ, during cell differentiation and in response to hormonal cues.

**Graded phosphatidylserine levels tune ROP6 signaling.**

In order to test the potential impact of phosphatidylserine variations during development, we experimentally manipulated the plant phosphatidylserine content, from no phosphatidylserine biosynthesis in the *phosphatidylserine synthase1* (*pss1*) mutant (*10*), to mild phosphatidylserine levels in transgenic lines expressing artificial microRNAs against *PSS1* (*amiPSS1*), and high phosphatidylserine levels in transgenic lines overexpressing *PSS1* (*PSS1-OX*) (Fig. S2). The changes in phosphatidylserine content measured in *amiPSS1* and *PSS1-OX* lines of about ±2-fold were in the physiological range, since phosphatidylserine levels in *Arabidopsis* vary about 5-fold between roots and leaves tissues (*19*). The *pss1* mutant showed defects in root gravitropism (Fig. S3A-B). Quantitative analyses of root bending following gravistimulation (Fig. S3C) revealed that the *pss1-3* mutant had no gravitropic response (Fig. 2A), *amiPSS1* lines had an attenuated response, while *PSS1-OX* lines were hypergravitropic (Fig. 2B). These opposite gravitropic phenotypes of *PSS1* loss- and gain-of-function resembled those of ROP6, a Rho-Of-Plant (ROP) GTPase, which is activated by auxin and regulates root gravitropism *(15, 16)*. Like *PSS1-OX* lines, lines overexpressing either ROP6 (*ROP6-OX*) or constitutive active GTP-lock ROP6 ($ROP6^{CA}$) showed a hypergravitropic phenotype, which were abolished in a *pss1-3* background (Fig 2A). During root gravitropism, ROP6 acts downstream of auxin to inhibit endocytosis and regulate microtubule orientation (*15*, *16*, *21*). Similar to *rop6 (15, 16, 21)*, we observed that in *pss1-3*: i) FM4-64 and PIN2-GFP uptake in the presence of BrefeldinA (BFA) was increased (Fig. 2C, Fig. S4A-D), ii) auxin failed to inhibit FM4-64 and PIN2-GFP endocytosis (Fig. 2C, Fig. S4A-D), iii) CLATHRIN-LIGHT-CHAIN plasma membrane association was insensitive to auxin treatment (Fig. S4E), and iv) auxin-triggered microtubule reorientation was abolished (Fig. S4F). FM4-64 uptake in *pss1-3xROP6*$^{CA}$ was identical to that of *pss1-3* single mutant and opposite to $ROP6^{CA}$ (Fig. 2C), showing that PSS1 is required for ROP6-mediated inhibition of endocytosis. Furthermore, transgenic lines with low phosphatidylserine content (*amiPSS1*) had decreased auxin-mediated inhibition of endocytosis, while lines with heightened-phosphatidylserine content (*PSS1-OX*) mimicked $ROP6^{CA}$ phenotypes with pronounced inhibition of endocytosis upon auxin treatment (Fig. 2D, Fig. S4G-I). Together, our analyses suggest that i) phosphatidylserine is required for auxin-mediated ROP6 signaling during root gravitropism and ii) phosphatidylserine levels impact the strength of ROP6 signaling output in a dose-dependent manner.

**Auxin triggers ROP6 nanoclustering.**

PS and ROP6 both accumulate at the plasma membrane, suggesting that phosphatidylserine may contribute to ROP6 localization. However, GFP-ROP6 localization, as seen by confocal

microscopy, was almost identical in *pss1-3* and wild-type plants, being mainly at the plasma membrane and only faintly delocalized in intracellular compartments in *pss1-3* (Fig. S5). In leaves, ROP6CA was previously shown to be confined in membrane domains (*22*), raising the possibility that phosphatidylserine could contribute to ROP6 signaling by regulating its lateral segregation at the plasma membrane. To analyze ROP6 plasma membrane partitioning in root cells and in the context of auxin response, we developed several microscopy-based assays, including Fluorescence Recovery After Photobleaching (FRAP), Total Internal Reflection Fluorescence Microscopy (TIRFM) and PhotoActivated Localization Microscopy (PALM) (Fig. S6). As shown for ROP6CA in leaf (*22*), activation of ROP6 (here using auxin treatment) delayed GFP-ROP6 fluorescence recovery after photobleaching in roots, and increased the proportion of immobile GFP-ROP6 (Fig. 3A and Fig. S7). TIRFM on root tip epidermal cells allowed to focus only on the plane of the plasma membrane with a 100nm axial resolution (Fig. S6B) and revealed that GFP-ROP6 mostly localized uniformly at the plasma membrane (Fig. 3B). By contrast, in auxin-treated plants (both with NAA or the naturally-occurring auxin indole-3-acetic acid, IAA), GFP-ROP6 additionally resided in diffraction-limited spots present in the plane of the plasma membrane (Fig. 3B and Fig. S8A), suggesting that auxin treatment triggers the clustering of ROP6 in membrane domains. By using stochastic photoswitching on live roots, single particle tracking PALM (sptPALM) experiments provided tracks of single molecule localization through time, and therefore allowed us to analyze the diffusion behavior of single ROP6 molecule in response to auxin (Fig. S6D). While mEos-ROP6 molecules in the untreated condition were almost exclusively diffusing, mEos-ROP6 molecules in plants treated for 5 minutes with NAA or IAA (or mEos-ROP6CA molecules) existed in two states at the plasma membrane of epidermal cells: immobile or diffusing (Fig. 3C-D, Fig. S9 and Supplementary Video 1). Clustering analyses on live PALM images (*23*) showed that auxin triggered the clustering of mEos-ROP6 in plasma membrane-nanodomains of about 50 to 70 nm wide (Fig. 3E-F and Fig. S10). Together, our data indicate that activation, either genetically (i.e. ROP6CA) or by an endogenous activator (i.e. auxin), triggers ROP6 recruitment, immobilization and stabilization into nanodomains and that these events happen minutes following auxin treatment.

**Dose-dependent regulation of ROP6 nanoclustering by phosphatidylserine.**

Next, we tested the impact of phosphatidylserine on ROP6 plasma membrane dynamics. In FRAP experiments, GFP-ROP6 sensitivity to auxin was reduced in *pss1-3* (Fig. 4A and Fig. S7), suggesting that phosphatidylserine is critical for the immobilization of ROP6 by auxin. In wild-type plants, NAA-induced GFP-ROP6 presence in nanodomains was more pronounced in the basal meristem than in the elongation zone in TIRFM experiments (Fig. 4B), which correlated with the observed differential presence of phosphatidylserine content at the plasma membrane in these regions (Fig. 1A). To analyze whether this differential auxin sensitivity was dependent on the amount of phosphatidylserine present in these cells, we performed phosphatidylserine loss- and gain-of-function experiments. First, auxin failed to induce GFP-ROP6 nanodomains in both region of the root in *pss1-3* (Fig. 4C), suggesting that phosphatidylserine is indeed required for auxin-triggered ROP6 nanoclustering. Second, exogenous treatment with lysophosphatidylserine, a more soluble lipid than phosphatidylserine but with an identical head group (*10*), boosted the number of auxin-induced GFP-ROP6 nanodomains observed in TIRFM in wild-type plants (Fig. S8B). Third, sptPALM analyses showed that the fraction of immobile mEos-ROP6CA (for which all ROP6 molecules are loaded with GTP) was significantly enhanced in *PSS1-OX* lines compared to the

wild type (Fig. 4D and Fig. S11). Together these data suggest that the quantity of phosphatidylserine at the plasma membrane impacts ROP6 nanoclustering.

While phosphatidylserine was required for auxin-triggered ROP6 nanoclustering, a certain amount of ROP6 was still found in plasma membrane domains in *pss1*, independent of the presence of auxin (Fig. 4C). Kymograph analyses revealed that ROP6-containing nanodomains observed by TIRFM in the presence of auxin were immobile in both wild-type and *pss1-3* background (Fig. 4E). Photobleaching experiments showed that GFP-ROP6 was highly stable in these nanodomains in the wild type (i.e. no fluorescence recovery of GFP-ROP6 in nanodomains, and fast recovery of fluorescence outside of these domains) (Fig. 4E and Supplementary Video 2). By contrast, GFP-ROP6 fluorescence in nanodomains was rapidly recovered in *pss1-3*, suggesting that ROP6 was not stabilized into nanodomains in the absence of phosphatidylserine (Fig. 4E and Supplementary Video 3). Together, our results show that phosphatidylserine is necessary for both ROP6 stabilization into nanodomains and downstream ROP6 signaling, including regulation of endocytosis and root gravitropism.

**Immobile phosphatidylserine molecules accumulate in nanodomains.**

Next, we addressed whether phosphatidylserine, like ROP6, also localizes in nanodomains. Using sptPALM and clustering analyses, we found that in both absence or presence of exogenous auxin: i) the phosphatidylserine reporter mEos-2xPH$_{EVCT2}$ segregated into nanodomains at the plasma membrane of root epidermal cells (Fig. 5A) and ii) about 50% of mEos-2xPH$_{EVCT2}$ molecules were present as a slow-diffusible population (Fig. 5B and Fig S12). mEos-2xPH$_{EVCT2}$ apparent diffusion coefficient in the absence and presence of auxin was similar to that of immobile mEos-ROP6 ROP6 in the presence of auxin (Fig. 3D), suggesting that ROP6 may cluster in preexisting PS nanodomains. Accordingly, co-visualization of GFP-ROP6 and the phosphatidylserine sensor 2xmCHERRY-C2$_{Lact}$ in TIRFM confirmed that they at least partially reside in the same nanodomains in response to auxin, while only 2xmCHERRY-C2$_{Lact}$ was present in nanocluster in the absence of auxin (Fig. 5C and S12D).

**Direct ROP6-lipid interactions control nanoclustering and signaling.**

ROP6 possess in its C-terminus a polybasic region adjacent to a prenylation site (Fig. S13A). Such polybasic region is anticipated to bind to anionic phospholipids, including phosphatidylserine (*3, 4, 6*), which we confirmed in protein-lipid overlay experiments (Fig. S13B). Substitution of seven lysines into neutral glutamines in ROP6 C-terminus (ROP6$_{7Q}$) abolished *in vitro* interactions with all anionic lipids (Fig. S13B). In planta, diminishing the net positive charges of ROP6 C-terminus or the net negative charge of the plasma membrane gradually induced ROP6 mislocalization into intracellular compartments (Fig. S13C-D). To test the functionality of ROP6$_{7Q}$ at the plasma membrane, we selected transgenic lines that had strong expression level to compensate for their intracellular localization and therefore have comparable levels of ROP6$_{7Q}$ and ROP6 at the plasma membrane (Fig. S14A and D-F). ROP6$_{7Q}$ mutants were not functional in planta (Fig. 5D-E, Fig. S14B-C), even though the 7Q mutations had no impact on ROP6 intrinsic GTPase activity *in vitro* and ROP6-GTP conformation in vivo (Fig. S15). We next analyzed the dynamics of mEos-ROP6$_{7Q}$ at the plasma membrane of wild-type roots by sptPALM experiments and found that it had the same proportion of immobile molecules than mEos-ROP6 in *pss1-3*, and that in both cases they were insensitive to auxin (Fig. 5F, Fig. S16). Therefore, impairing PS/ROP6 interaction by either removing phosphatidylserine from the membranes (*pss1* mutant), or by mutating the anionic lipid-

binding site on ROP6 ($ROP6_{7Q}$) similarly impacted ROP6 signaling and its auxin-induced nanoclustering.

**Conclusions.**

Here, we showed that in root tip epidermal cells: i) ROP6 is immobilized in plasma membrane localized nanodomains upon activation by auxin, ii) phosphatidylserine is necessary for both ROP6 stabilization into nanodomains and signaling, iii) ROP6 directly interacts with anionic lipids, including phosphatidylserine, and iv) phosphatidylserine itself is present and immobile in these nanodomains, suggesting that stabilized ROP6 in phosphatidylserine-containing nanoclusters constitutes the functional signaling unit of this GTPase. Our imaging pipeline revealed that ROP6 nano-organization is rapidly remodeled by auxin and as such will provide a quantitative in vivo read-out to re-evaluate how auxin may be perceived upstream of ROP6 activation. Plants have 11 ROPs, which can respond to a wide range of signals (*11*), raising the question whether nanoclustering is specific to auxin response or common to other signals and to various ROPs, and to what extent it may contribute to signal integration by plant Rho GTPases. All ROP proteins have polybasic clusters at their C-terminus (Fig. S17A), and phosphatidylserine could therefore potentially regulate additional member of this family. In addition to root gravitropic defects, *pss1* had many developmental phenotypes that may be linked to altered ROP function (e.g. pavement cell and root hair morphology, planar polarity defects, see Fig. S17B-F) but that are not found in *rop6* single mutant and could therefore involve additional ROP proteins. Furthermore, we found that ROP6 interacts with phosphoinositides and phosphatidic acid, which are required for its proper targeting to the plasma membrane (Fig. S13). Additional studies are required to determine whether these anionic phospholipids may participate to ROP nanoclustering, perhaps in synergy with phosphatidylserine. Nanoclustering is a shared feature of several yeast and animal small GTPases, including K-Ras, Rac1 and Cdc42 (*5-8*), and both K-Ras and Cdc42 require phosphatidylserine for nanoclustering (*2*, *6-8*). Here, we showed the dependence of ROP6 function on PS level. This opens the possibility that variations of the phosphatidylserine concentration at the plasma membrane of both animal and plant systems may have specific regulatory functions and could control the signaling capacity of small GTPases during either normal or pathological development.

**References and Notes:**


1. S. Etienne-Manneville, A. Hall, Rho GTPases in cell biology. *Nature* **420**, 629-635 (2002).
2. Y. Zhou, J. F. Hancock, Deciphering lipid codes: K-Ras as a paradigm. *Traffic* **19**, 157-165 (2018).
3. W. D. Heo *et al.*, PI(3,4,5)P3 and PI(4,5)P2 lipids target proteins with polybasic clusters to the plasma membrane. *Science* **314**, 1458-1461 (2006).
4. T. Yeung *et al.*, Membrane phosphatidylserine regulates surface charge and protein localization. *Science* **319**, 210-213 (2008).
5. A. Remorino *et al.*, Gradients of Rac1 Nanoclusters Support Spatial Patterns of Rac1 Signaling. *Cell reports* **21**, 1922-1935 (2017).
6. Y. Zhou *et al.*, Lipid-Sorting Specificity Encoded in K-Ras Membrane Anchor Regulates Signal Output. *Cell* **168**, 239-251 e216 (2017).

7. E. Sartorel *et al.*, Phosphatidylserine and GTPase activation control Cdc42 nanoclustering to counter dissipative diffusion. *Molecular biology of the cell*, mbcE18010051 (2018).
8. J. Meca *et al.*, Avidity-driven polarity establishment via multivalent lipid-GTPase module interactions. *The EMBO journal*, (2018).
9. P. A. Leventis, S. Grinstein, The distribution and function of phosphatidylserine in cellular membranes. *Annual review of biophysics* **39**, 407-427 (2010).
10. M. P. Platre *et al.*, A Combinatorial Lipid Code Shapes the Electrostatic Landscape of Plant Endomembranes. *Developmental cell* **45**, 465-480 e411 (2018).
11. G. Feiguelman, Y. Fu, S. Yalovsky, ROP GTPases Structure-Function and Signaling Pathways. *Plant physiology* **176**, 57-79 (2018).
12. L. Z. Tao, A. Y. Cheung, H. M. Wu, Plant Rac-like GTPases are activated by auxin and mediate auxin-responsive gene expression. *The Plant cell* **14**, 2745-2760 (2002).
13. T. Xu *et al.*, Cell surface- and rho GTPase-based auxin signaling controls cellular interdigitation in Arabidopsis. *Cell* **143**, 99-110 (2010).
14. Q. Duan, D. Kita, C. Li, A. Y. Cheung, H. M. Wu, FERONIA receptor-like kinase regulates RHO GTPase signaling of root hair development. *Proceedings of the National Academy of Sciences of the United States of America* **107**, 17821-17826 (2010).
15. X. Chen *et al.*, ABP1 and ROP6 GTPase signaling regulate clathrin-mediated endocytosis in Arabidopsis roots. *Current biology : CB* **22**, 1326-1332 (2012).
16. D. Lin *et al.*, A ROP GTPase-dependent auxin signaling pathway regulates the subcellular distribution of PIN2 in Arabidopsis roots. *Current biology : CB* **22**, 1319-1325 (2012).
17. T. Xu *et al.*, Cell surface ABP1-TMK auxin-sensing complex activates ROP GTPase signaling. *Science* **343**, 1025-1028 (2014).
18. L. Poraty-Gavra *et al.*, The Arabidopsis Rho of plants GTPase AtROP6 functions in developmental and pathogen response pathways. *Plant physiology* **161**, 1172-1188 (2013).
19. Y. Yamaoka *et al.*, PHOSPHATIDYLSERINE SYNTHASE1 is required for microspore development in Arabidopsis thaliana. *The Plant journal : for cell and molecular biology* **67**, 648-661 (2011).
20. M. L. Simon *et al.*, A PtdIns(4)P-driven electrostatic field controls cell membrane identity and signalling in plants. *Nat Plants* **2**, 16089 (2016).
21. X. Chen *et al.*, Inhibition of cell expansion by rapid ABP1-mediated auxin effect on microtubules. *Nature* **516**, 90-93 (2014).
22. N. Sorek *et al.*, An S-acylation switch of conserved G domain cysteines is required for polarity signaling by ROP GTPases. *Current biology : CB* **20**, 914-920 (2010).
23. J. Gronnier *et al.*, Structural basis for plant plasma membrane protein dynamics and organization into functional nanodomains. *eLife* **6**, (2017).
24. I. A. Sparkes, J. Runions, A. Kearns, C. Hawes, Rapid, transient expression of fluorescent fusion proteins in tobacco plants and generation of stably transformed plants. *Nature protocols* **1**, 2019-2025 (2006).
25. M. L. Simon *et al.*, A multi-colour/multi-affinity marker set to visualize phosphoinositide dynamics in Arabidopsis. *The Plant journal : for cell and molecular biology* **77**, 322-337 (2014).

26. K. Elsayad *et al.*, Mapping the subcellular mechanical properties of live cells in tissues with fluorescence emission-Brillouin imaging. *Science signaling* **9**, rs5 (2016).
27. C. A. Konopka, S. K. Backues, S. Y. Bednarek, Dynamics of Arabidopsis dynamin-related protein 1C and a clathrin light chain at the plasma membrane. *The Plant cell* **20**, 1363-1380 (2008).
28. J. Xu, B. Scheres, Dissection of Arabidopsis ADP-RIBOSYLATION FACTOR 1 function in epidermal cell polarity. *The Plant cell* **17**, 525-536 (2005).
29. E. Hosy, A. Martiniere, D. Choquet, C. Maurel, D. T. Luu, Super-resolved and dynamic imaging of membrane proteins in plant cells reveal contrasting kinetic profiles and multiple confinement mechanisms. *Molecular plant* **8**, 339-342 (2015).
30. A. Martiniere *et al.*, Cell wall constrains lateral diffusion of plant plasma-membrane proteins. *Proceedings of the National Academy of Sciences of the United States of America* **109**, 12805-12810 (2012).
31. A. Martiniere, P. Gayral, C. Hawes, J. Runions, Building bridges: formin1 of Arabidopsis forms a connection between the cell wall and the actin cytoskeleton. *The Plant journal : for cell and molecular biology* **66**, 354-365 (2011).
32. C. A. Schneider, W. S. Rasband, K. W. Eliceiri, NIH Image to ImageJ: 25 years of image analysis. *Nature methods* **9**, 671-675 (2012).
33. A. Serge, N. Bertaux, H. Rigneault, D. Marguet, Dynamic multiple-target tracing to probe spatiotemporal cartography of cell membranes. *Nature methods* **5**, 687-694 (2008).
34. A. Martinière *et al,* Osmotic stress activates two ROS pathways with distinct impacts on protein nanodomains and diffusion. *Plant Physiology* **in press**, (2019).
35. H. Yoshizaki *et al.*, Activity of Rho-family GTPases during cell division as visualized with FRET-based probes. *The Journal of cell biology* **162**, 223-232 (2003).
36. K. Kurokawa, R. E. Itoh, H. Yoshizaki, Y. O. Nakamura, M. Matsuda, Coactivation of Rac1 and Cdc42 at lamellipodia and membrane ruffles induced by epidermal growth factor. *Molecular biology of the cell* **15**, 1003-1010 (2004).
37. R. E. Itoh *et al.*, Activation of rac and cdc42 video imaged by fluorescent resonance energy transfer-based single-molecule probes in the membrane of living cells. *Molecular and cellular biology* **22**, 6582-6591 (2002).
38. A. Akamatsu *et al.*, An OsCEBiP/OsCERK1-OsRacGEF1-OsRac1 module is an essential early component of chitin-induced rice immunity. *Cell host & microbe* **13**, 465-476 (2013).
39. M. M. Marques-Bueno *et al.*, A versatile Multisite Gateway-compatible promoter and transgenic line collection for cell type-specific functional genomics in Arabidopsis. *The Plant journal : for cell and molecular biology* **85**, 320-333 (2016).
40. Y. Jaillais *et al.*, Tyrosine phosphorylation controls brassinosteroid receptor activation by triggering membrane release of its kinase inhibitor. *Genes & development* **25**, 232-237 (2011).
41. M. Karimi, A. Bleys, R. Vanderhaeghen, P. Hilson, Building blocks for plant gene assembly. *Plant physiology* **145**, 1183-1191 (2007).
42. K. Nito, C. C. Wong, J. R. Yates, 3rd, J. Chory, Tyrosine phosphorylation regulates the activity of phytochrome photoreceptors. *Cell reports* **3**, 1970-1979 (2013).
43. A. M. Heape, H. Juguelin, F. Boiron, C. Cassagne, Improved one-dimensional thin-layer chromatographic technique for polar lipids. *J Chromatogr* **322**, 391-395 (1985).

44. L. J. Macala, R. K. Yu, S. Ando, Analysis of brain lipids by high performance thin-layer chromatography and densitometry. *Journal of lipid research* **24**, 1243-1250 (1983).
45. J. Schindelin *et al.*, Fiji: an open-source platform for biological-image analysis. *Nature methods* **9**, 676-682 (2012).
46. A. French, S. Ubeda-Tomas, T. J. Holman, M. J. Bennett, T. Pridmore, High-throughput quantification of root growth using a novel image-analysis tool. *Plant physiology* **150**, 1784-1795 (2009).
47. A. Grabov *et al.*, Morphometric analysis of root shape. *The New phytologist* **165**, 641-651 (2005).
48. A. Boudaoud *et al.*, FibrilTool, an ImageJ plug-in to quantify fibrillar structures in raw microscopy images. *Nature protocols* **9**, 457-463 (2014).
49. V. Bayle, M. P. Platre, Y. Jaillais, Automatic Quantification of the Number of Intracellular Compartments in Arabidopsis thaliana Root Cells. *Bio-protocol* **7**, (2017).
50. F. Levet *et al.*, SR-Tesseler: a method to segment and quantify localization-based super-resolution microscopy data. *Nature methods* **12**, 1065-1071 (2015).
51. A. Johnson, G. Vert, Single Event Resolution of Plant Plasma Membrane Protein Endocytosis by TIRF Microscopy. *Frontiers in plant science* **8**, 612 (2017).
52. K. Maeda *et al.*, Interactome map uncovers phosphatidylserine transport by oxysterol-binding proteins. *Nature* **501**, 257-261 (2013).
53. J. Chung *et al.*, PI4P/phosphatidylserine countertransport at ORP5- and ORP8-mediated ER-plasma membrane contacts. *Science* **349**, 428-432 (2015).
54. J. Moser von Filseck *et al.*, Phosphatidylserine transport by ORP/Osh proteins is driven by phosphatidylinositol 4-phosphate. *Science* **349**, 432-436 (2015).
55. R. Raghupathy *et al.*, Transbilayer lipid interactions mediate nanoclustering of lipid-anchored proteins. *Cell* **161**, 581-594 (2015).
56. T. Yeung *et al.*, Receptor activation alters inner surface potential during phagocytosis. *Science* **313**, 347-351 (2006).
57. G. R. Hammond *et al.*, PI4P and PI(4,5)P2 are essential but independent lipid determinants of membrane identity. *Science* **337**, 727-730 (2012).

**Acknowledgments:** We thank M. Dreux, E. Bayer, O. Hamant, S. Mongrand, Y. Boutté, J. Gronnier, J. Reed, T. Vernoux and the SiCE group for discussions and comments, T. Stanislas for help with root hair phenotyping, C. Burny for help with statistics, B. Peret for sharing his root template, S. Bednarek, S. Yalovsky, B. Scheres and the NASC collection for providing transgenic *Arabidopsis* lines, A. Lacroix, J. Berger and P. Bolland for plant care, J.C. Mulatier for help in preparing lipids. We acknowledge the contribution of SFR Biosciences (UMS3444/CNRS, US8/Inserm, ENS de Lyon, UCBL) facilities: C. Lionnet, E. Chattre, and C. Chamot at the LBI-PLATIM-MICROSCOPY for assistance with imaging and V. Guegen-Chaignon at the Protein Science Facility for assistance with protein purification. We thank the PHIV and MRI platform for access to microscopes. **Funding:** Y.J. is funded by ERC no. 3363360-APPL under FP/2007-2013; Y.J and A.M. by the innovative project *iRhobot* from the department of "Biologie et Amélioration des Plantes" (BAP) of INRA. **Author contributions:** M.P.P. generated all transgenic material, and was responsible for all experiments. V.B., M.P.P. and A.M. conceived, performed and analyzed super-resolution imaging. V.B. performed and analyzed TIRFM and FRAP imaging. L.M-P and P.M. performed lipid measurements. A.M. imaged Raichu-ROP6 sensors. J.B. produced recombinant ROP6 and performed GTPase assays. M.P.P and L.A. performed lipid

overlay experiments. M.M.M-B., and C.M. assisted with phenotyping and cloning, A.C. performed qRT-PCR analyses, J-B.F. and M.N. designed the sptPALM analyses pipeline, M.P.P., V.B. and Y.J. conceived the study, designed experiments and wrote the manuscript and all the authors discussed the results and commented on the manuscript. Correspondence and requests for materials should be addressed to Y.J. **Competing interests:** Authors declare no competing interests. **Data and materials availability:** All data is available in the main text or the supplementary materials

**Supplementary Materials:**

Materials and Methods

Figures S1-S17

Movies S1-S3

References (*24-57*)

**Figures**

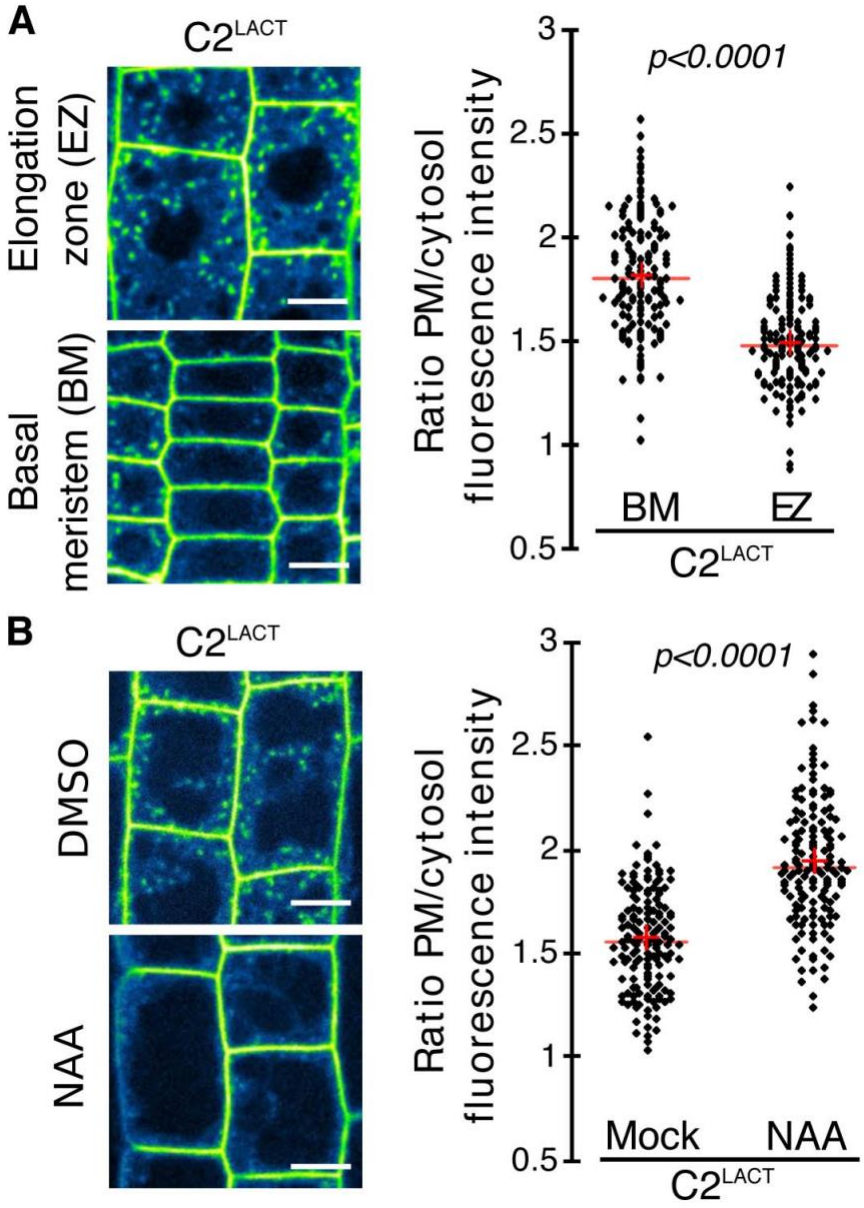


**Figure 1. Plasma membrane phosphatidylserine levels vary during root cell differentiation.** **A-B** Confocal images and quantification of the plasma membrane (PM)/cytosol ratio of mCIT-C2LACT (phosphatidylserine (PS) sensor) root epidermis in: (A) basal meristem (BM) and elongation zone (EZ) and (B) absence/presence of NAA (10µM, 60min), (*n=150* cells). Scale bars 10µm. Red crosses represent the mean, red lines the median, letters indicate statistical differences (see methods for details on statistical tests).

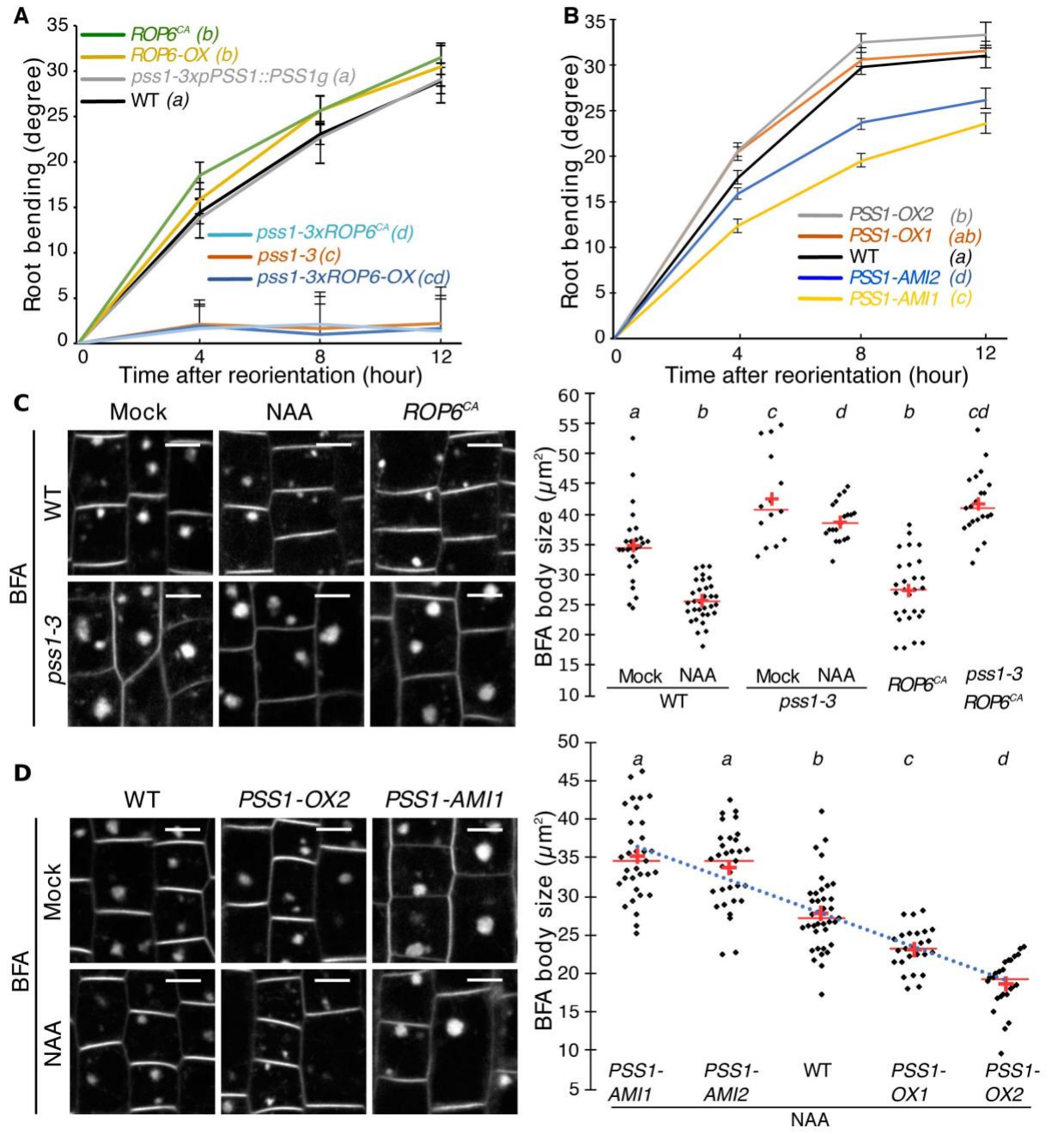


**Figure 2. Variation in phosphatidylserine concentration tunes ROP6-mediated auxin response. A-B**, Quantification of root bending after gravistimulation (mean +/- sem, from top: *n=40,28,39,33,70,64,51* in A, *n=40,52,65,77,57* in B)). **C-D**, Confocal images of FM4-64 staining in root epidermis (BFA: 25µM; NAA: 5µM), and related quantification (*n=26,37,14,21,28,21* in C, *n=33,32,36,25,24* in D). Scale bars 10µm. Red crosses represent the mean, red lines the median, doted blue line the tendency curve, *n* the number of roots analyzed, letters indicate statistical differences (see methods for details on statistical tests).

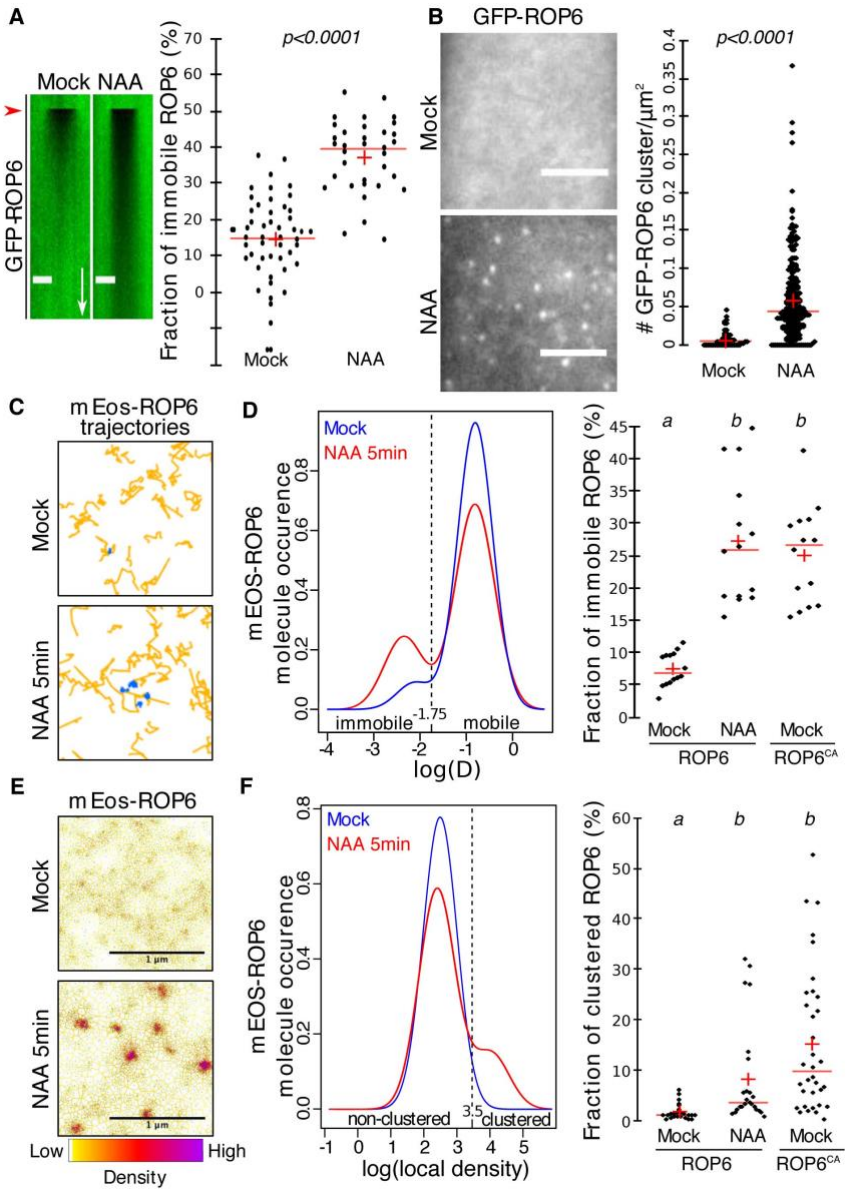


**Figure 3. Auxin triggers ROP6 nanoclustering at the plasma membrane of root epidermal cells. A**, kymograph images of GFP-ROP6 during FRAP experiments (NAA: 100nM, 30 min), and quantification of GFP-ROP6 immobile fraction determine by FRAP analyzes (*n=48,34*). Red arrowhead indicates bleaching and white arrow is a 9s timescale. **B**, TIRFM micrograph of GFP-ROP6 (NAA: 10µM, 20 min) and related quantification (*n=151,277*). **C**, Representative mEos-ROP6 trajectories obtained by sptPALM analyses. Immobile molecules are in blue, mobile molecules in orange. **D**, Distribution of mEos-ROP6 molecules according to their apparent diffusion coefficient obtained by analyzing sptPALM trajectories (NAA: 10µM, 5 min), and related quantification (*n=14,14,14*). **E**, Live PALM analysis of mEos-ROP6 molecules density by tessellation-based automatic segmentation of super-resolution images (NAA: 10µM, 5 min). **F**, Distribution of mEos-ROP6 molecules according to their local density and related quantification (*n=24,24,34*). Scale bars: 5 µm (A-B), 1 µm (E). Red crosses represent the mean, red lines the median, *n* the number of ROIs (A, B), or independent acquisitions (different cells) (D and F) analyzed, letters indicate statistical difference (see methods for details on statistical tests).

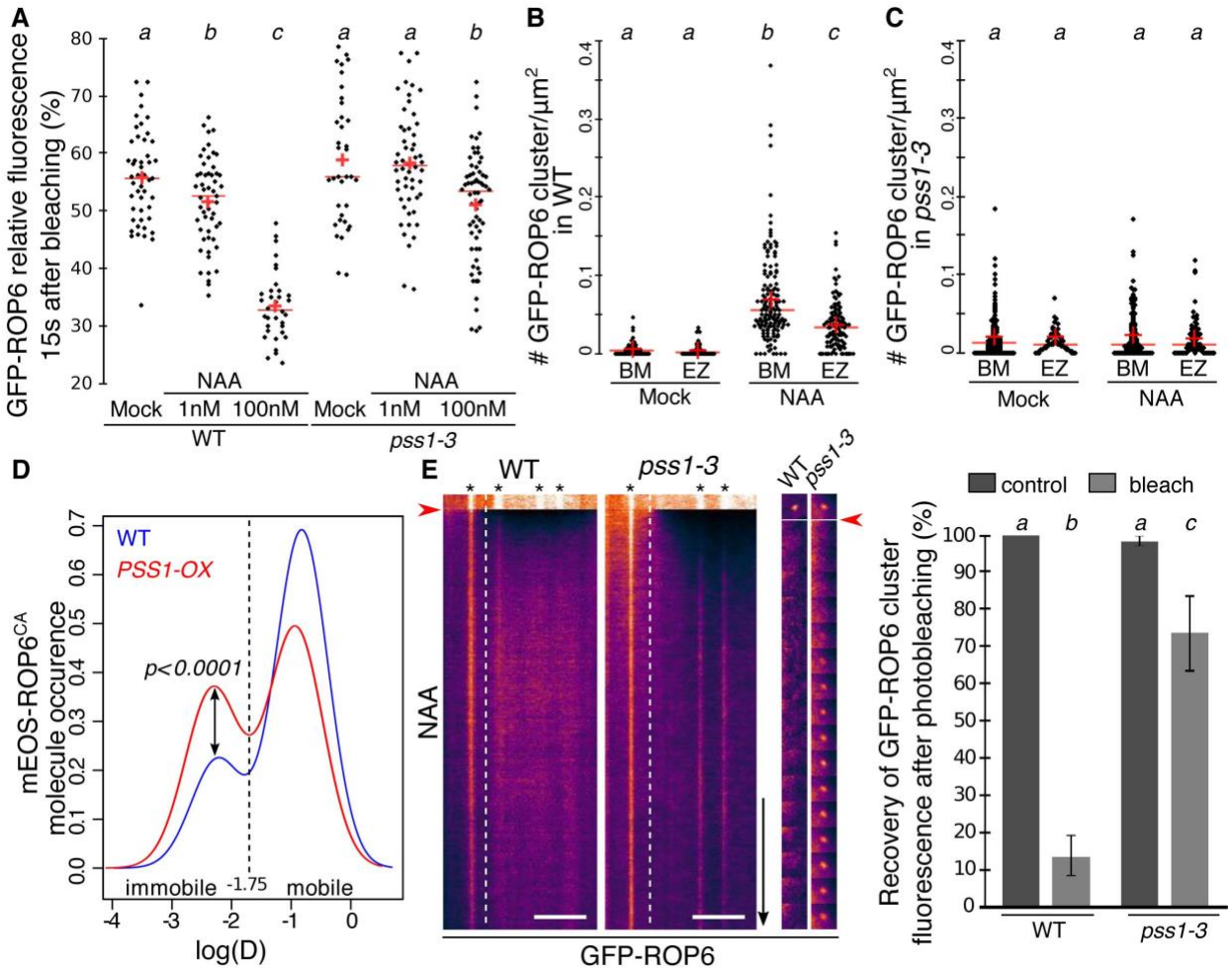


**Figure 4. Phosphatidylserine is necessary for auxin-induced stabilization of ROP6 into nanodomains. A**, Quantification of FRAP experiments in wild-type (WT) and *pss1-3* root epidermal cells (NAA: 1nM and 100nM, 30 min, *n=48,54,34,36,54,64*). **B-C**, Quantification of TIRFM experiment in WT (*n=65,78,149,116*) and *pss1-3* (*n=68,170,73,168*) root epidermal cells (NAA, 10µM, 20 min) in basal meristem (BM) and elongation zone (EZ) (data are the same as in Fig3B but split into its respective zone). **D**, Distribution of mEos-ROP6CA molecules according to their apparent diffusion coefficient obtained by analyzing sptPALM trajectories in the wild-type (WT) and *PSS1-OX* background (*n=18,18*). **E**, Kymograph of GFP-ROP6 localization obtained by TIRFM, with images of a single GFP-ROP6 nanocluster (9s interval) and related quantification (*n=282,121,195,91*). The black arrow is a 12s timescale, the red arrowhead indicates bleaching, * indicates GFP-ROP6-containing nanodomains. Scale bars: 5 µm. Red crosses represent the mean, red lines the median, *n* the number of ROIs (A-C), independent acquisition (D) or GFP-ROP6 nanodomains (E) analyzed, letters indicate statistical difference (see methods for details on statistical tests).

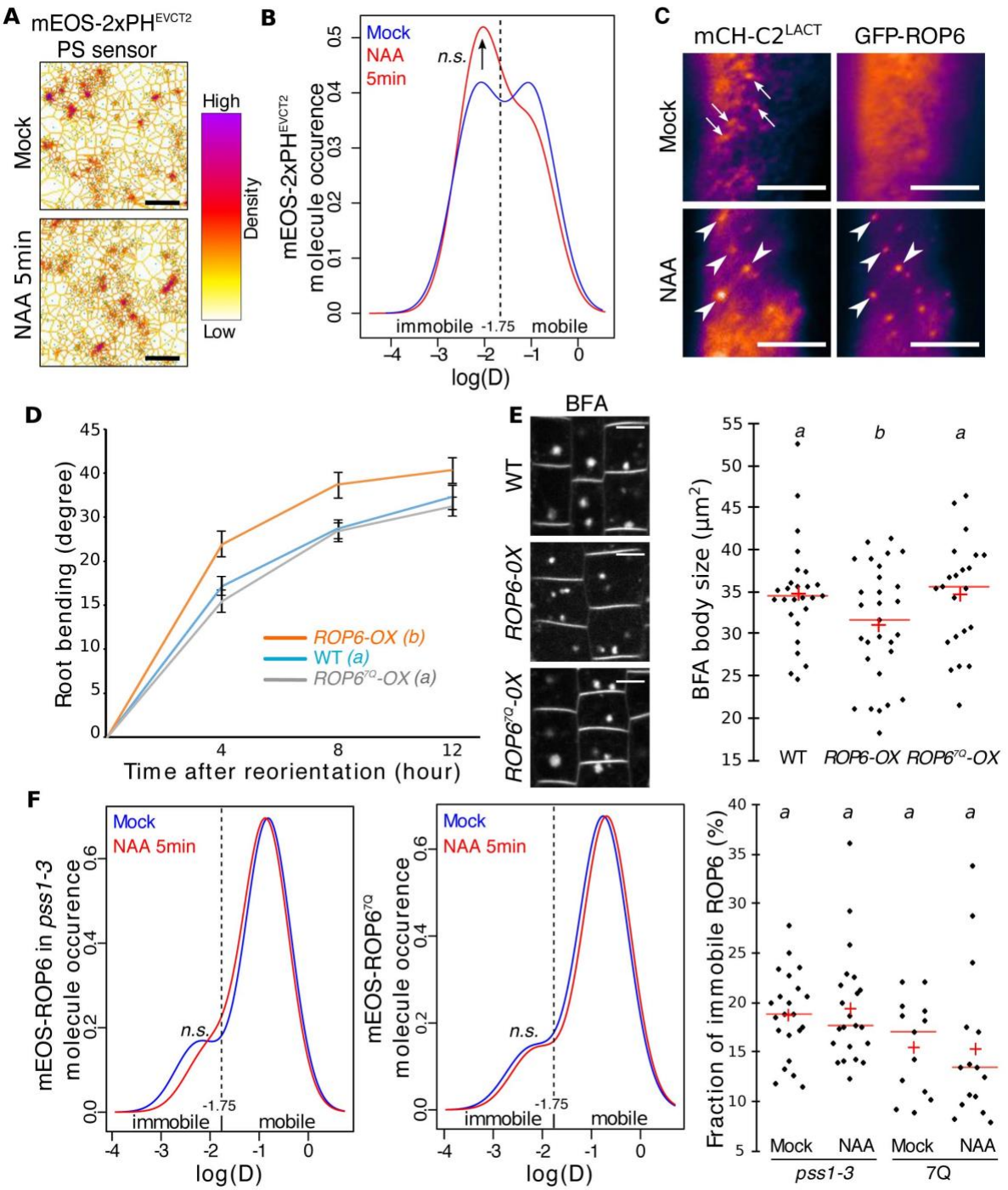


**Figure 5. ROP6 nanoclustering in response to auxin and downstream signaling requires interaction with anionic phospholipids**. **A**, Live PALM analysis of mEos-2xPH$_{EVCT2}$ molecules density by tessellation-based automatic segmentation of super-resolution images (NAA, 10µM, 5 min) in root epidermal cells and **B**, distribution of mEos-2xPH$_{EVCT2}$ molecules according to their apparent diffusion coefficient obtained by analyzing sptPALM trajectories (*n=24,34*). **C**, TIRFM micrograph of root cells co-expressing GFP-ROP6 with the phosphatidylserine marker 2xmCH-C2$_{LACT}$ (NAA: 10µM, 20 min). Arrow indicates PS-containing nanodomains in the absence of auxin, arrowheads indicate PS- and ROP6-containing nanodomains in the presence of auxin. **D-E**,

Quantification of (D) root bending after gravistimulation (*n=49,43,42*) and (E) the size of FM4-64-stained BFA bodies (data in wild type (WT) are the same as in Figure 2C, *n=26,29,22*). **F**, Distribution of mEos-ROP6 molecules in *pss1-3* (left) and mEos-ROP6$^{7Q}$ molecules in wild-type (WT) (right) roots according to their apparent diffusion coefficient obtained by analyzing sptPALM trajectories (NAA: 10µM, 5 min), and related quantification (*n=22,22,13,15*). Scale bars 1µm (A), 5µm (C), 10µm (E). Red crosses represent the mean, red lines the median, *n* the number of acquisitions (independent cells) (B, F) or roots analyzed (D-E), letter indicates statistical difference (see methods for details on statistical tests).

# Supplementary Materials for

## Developmental control of plant Rho GTPase nano-organization by the lipid phosphatidylserine

Matthieu Pierre Platre, Vincent Bayle, Laia Armengot, Joseph Bareille, Maria Mar Marques-Bueno, Audrey Creff, Lilly Maneta-Peyret, Jean-Bernard Fiche, Marcelo Nolmann, Christine Miège, Patrick Moreau, Alexandre Martinière and Yvon Jaillais

correspondence to: yvon.jaillais@ens-lyon.fr

**This PDF file includes:**



**Other Supplementary Materials for this manuscript includes the following:**

## Materials and Methods

Growth condition and plant materials.

*Arabidopsis thaliana* Col-0 accession was used as the wild-type (WT) reference background throughout this study. Plants were grown in soil under long-day conditions at 21°C and 70% humidity and *in vitro* on Murashige and Skoog (MS) Basal Medium supplemented with 0.8% plant agar (pH 5.7) in continuous light conditions at 21°C. Every plant used for experiments are homozygous lines or F2 crosses. *Nicotiana tabacum* cv. Petit Havana plants were grown and used in transient transformation experiments as described (*24*). The following lines were published before: *pss1-3, pss1-4, pss1-5, pss1-3xPSS1prom::PSS1genomic; UBQ10prom::mCHERRY-C2$_{Lact}$ (NASC# N2107778), UBQ10prom::mCITRINE-2xPH$_{EVCT2}$ (NASC# N2107779), UBQ10prom::mCITRINE-1xPASS (NASC# N2107781)* (*10*)*; UBQ10prom::mCITRINE-C2$_{Lact}$ (NASC# N2107347), UBQ10prom::mCITRINE-KA1$_{MARK1}$ (NASC# N2107345), UBQ10prom::mCITRINE-P4M (NASC# N2107346)* (*20*)*; UBQ10prom::mCITRINE-2xPH$_{FAPP1}$ (NASC# N2105607), UBQ10prom::mCITRINE-2xPH$_{PLC}$ (NASC# N2105613), UBQ10prom::mCITRINE-TUBBY-C (NASC# N2105610) (25); UBQ10prom::2xmCHERRY-Lti6b (26); 35Sprom::GFP-ROP6, 35Sprom::GFP-ROP6$_{CA}$* (*22*)*; rop6-2* (*16*)*;CLC2prom::CLC2-GFP* (*27*)*; 35S::GFP-TUA6 (NASC# N6551); PIN2prom::PIN2-GFP* (*28*)*; UBQ10prom::PIP2a-mEos* (*29*).

Microscopy setup.

All imaging experiments were performed with the following spinning disk confocal microscope set up, except when indicated otherwise (see below): inverted Zeiss microscope (AxioObserver Z1, Carl Zeiss Group, http://www.zeiss.com/) equipped with a spinning disk module (CSU-W1-T3, Yokogawa, www.yokogawa.com) and a ProEM+ 1024B camera (Princeton Instrument, http://www.princetoninstruments.com/) using a 63x Plan-Apochromat objective (numerical aperture 1.4, oil immersion). GFP was excited with a 488nm laser (150mW) and fluorescence emission was filtered by a 525/50 nm BrightLine® single-band bandpass filter (Semrock, http://www.semrock.com/). YFP/mCITRINE were excited with a 515nm laser (60mW) and fluorescence emission was filtered by a 578/105nm BrightLine® single-band bandpass filter (Semrock, http://www.semrock.com/). mCHERRY and FM4-64 were excited with a 561nm laser (80 mW) and fluorescence emission was filtered by a 609/54 nm BrightLine® single-band bandpass filter (Semrock, http://www.semrock.com/). 488 or 515nm lasers were used to excite GFP or YFP/mCITRINE. For quantitative imaging, pictures of epidermal root meristem cells were taken with detector settings optimized for low background and no pixel saturation. Care was taken to use similar confocal settings when comparing fluorescence intensity or for quantification.

Tabaco leaves expressing raichu FRET sensors were observed with an inverted Leica SP8 laser scanning microscope using a 40x Plan-Apochromat objective (numerical aperture 1.1, water immersion). Fluorescent proteins were excited with 458 nm line of a Ne-Ag laser and light were collected simultaneously from 467 to 493 nm for CFP channel and from 538 to 573 for YFP channel. The HyD spectral detector was set to avoid bleed through of CFP fluorescence in the YFP$_{FRET}$ channel. A pinhole of 1 Airy unit was defined. Pixel size and dwell time was respectively 0.143µm and 1.2µs. Those settings were defined to record no signal on non-transformed leaves and kept similar for Raichu constructs tested.

FRAP experiments.

Fluorescence in a rectangle region of interest (ROI) (50 $\mu m^2$, 15 µm long) was bleached in the plasma membrane optical section by four successive scans at full laser power (150 W) using the iLas2 FRAP module (Roper scientific, http://www.biovis.com/ilas.htm) of our spinning disc microscope (cf description of the system above). FRAP was recorded continuously during 90 s with a delay of 0.3 s between frames. Fluorescence recovery was subsequently analyzed in the bleached ROIs and in controlled ROIs (rectangle with the same dimension in unbleached area). Fluorescence intensity of an ROI (same size as the bleached region) was systematically measured outside the root and subtracted to plasma membrane as background correction. Fluorescence intensity data were normalized as previously described (*30, 31*). Briefly, fluorescence intensity data were normalized using the equation: $I_n=[(I_t-I_{min})/(I_{max}-I_{min})]x100$. Where $I_n$ is the normalized intensity, $I_t$ is the intensity at any time t, $I_{min}$ is the minimum post-photobleaching intensity and $I_{max}$ is the mean pre-photobleaching intensity. Normalized recovery data were then fitted to an exponential recovery fitting curve using the Curve Fitting Tool in ImageJ (https://imagej.nih.gov/ij/) (*32*). Fitted coefficient were then used to calculate halftime of recovery as the time at which fluorescence intensity reaches half of the final recovered intensity. In graphs, relative to halftime of recovery after photobleaching, "n" represents the number of regions of interest (ROI) used for quantification.

TIRF and FRAP experiments in TIRF mode.

Total Internal Reflection Fluorescence (TIRF) Microscopy was done using the inverted Zeiss microscope previously described (AxioObserver Z1) equipped with azimuthal-TIRF iLas2 system (Roper Scientific) and a 100x Plan-Apochromat objective (numerical aperture 1.46, oil immersion). Pixel size was 0.13µm. The azimuth calibration was performed using the manufacturer recommendation and the iLas2 module in Metamorph software. The optimum critical angle was determined as giving the best signal-to-noise ratio. Images were acquired with 200ms exposure time, and 300ms between frames in time-lapse experiments. The photobleaching of ROP6 microdomains was achieved on circular ROIs (15µm diameter) by two successive scans at full laser power (150 W) using the iLas2 FRAP module. Pre- and post-acquisitions were recorded in TIRF during 5 minutes with a delay of 0.3 s between frames. In graphs, relative to domain recovery after photobleaching, "n" represents the number of regions of interest (ROI) used for quantification.

sptPALM.

Imaging was performed on a Zeiss Elyra PS1 system with a 100x Apo (numerical aperture 1.46 Oil objective), in TIRF mode. The optimum critical angle was determined as giving the best signal-to-noise ratio. Pixel size was 0.107µm. mEOS was photoconverted using 405nm UV laser power and resulting photoconverted fluorophores were excited using 561nm laser. UV laser power was adjusted to have significant number of tracks without too high density to facilitate further analyses (0.01 to 0.08%). 10,000 images time series were recorded at 50 frames per second (20ms exposure time) on a 256 x 256-pixel region of interest. Single molecule detection and tracks reconstruction were made using MTT algorithm (*33*) and further computational analyses of tracks were made using CBS sptPALM analyzer (*34*).

FM4-64, BFA, NAA, IAA, PAO, R59022 and lysophosphatidylserine treatments.

For BFA body size quantification, the plasma membrane and endosomes of 7 to 10-day old transgenic lines were stained by incubating roots with 1 µM FM4-64 (thermofisher scientific, https://www.thermofisher.com) concomitantly with Brefeldin A at 25 µM (BFA, Sigma, www.sigmaaldrich.com, BFA stock solution at 50 mM in DMSO) in liquid MS solution for 60 min. For the auxin analog, Naphthaleneacetic acid (NAA) effect on BFA body size, plants were pretreated with NAA for 30 minutes at 5 µM (Sigma, http://www.sigmaaldrich.com/, NAA stock at 10 mM in DMSO) and then the plasma membrane and endosomes of 5 to 10-day old transgenic lines were stained by incubating roots with 1 µM FM4-64 concomitantly with BFA at 25 µM and NAA at 5 µM in liquid MS solution for 60 min. For NAA effect on microtubule orientation, 10-12-day old seedlings expressing GFP-TUA6 were treated with NAA at 100 nM for 60 minutes. NAA at 5 µM for 30 minutes was applied on 10 to 12-day old seedlings to quantify the percentage of cell showing CLC2 at the plasma membrane. For PIN2 endocytosis, transgenic lines expressing PIN2-GFP (10 to 12 days-old seedlings), were treated with BFA at the indicated time (60 min or 120 min) and concentration (10µM, 25µM or 50µM) in 12-well plates. For NAA effect on endocytosis, PIN2-GFP expressing lines were pretreated with NAA at 10 µM for 30 minutes and then concomitantly treated with NAA at 10 µM and BFA at 50 µM for 60 min in 12-well plates. For NAA effect on phosphatidylserine biosensors *mCITRINE-C2$_{LACT}$* and *mCITRINE-2xPH$_{EVCT2}$*, 5 to 7-day old seedlings were treated with 10 µM NAA for 60 min. 5 to 7 day old seedlings expressing *35Sprom::GFP-ROP6 (GFP-ROP6)*, *ROP6prom::mCITRINE-ROP6* (mCit-ROP6) and *UBQ10prom::mCITRINE-ROP6-c-term* (mCit-ROP6$_{Cter}$) were incubated in wells containing 12.5 µM R59022 for 60 min or PAO at 30µM for 30 minutes. Plants observed in TIRFM were treated with NAA at 100nM or 10µM for 20 minutes, or IAA at 100nM for 20 minutes (IAA stock at 10mM in DMSO). For sptPALM experiment, plants were incubated in DMSO for 20 minutes in 12-well plates and then NAA or IAA treatment was performed at 10µM (stock solution 100mM in DMSO) for 5 minutes. For FRAP experiment, NAA was applied at 1nm and 100nm for 30 min. For each treatment, the mock condition corresponds to incubation of plants in well supplemented with a volume of DMSO equivalent to the highest drug/hormone concentration used and for the same time as the actual treatment. Roots were imaged within a 5-minute time frame window around the indicated time. Lysophosphatidylserine treatments were performed as described (*10*).

Cloning: preparation of gateway compatible entry clones (entry vector).
Published gateway compatible entry vectors are listed below.

The *ROP6* promoter (*ROP6prom*) was amplified from *Col0* genomic DNA. Gateway compatible PCR products were introduced into *pDONRP4R-P1* vectors (Thermofisher, www.thermofisher.com, cat# 12537023) by BP recombination using the following primers: *ROP6prom_F* (ttttttgtacaaacttgcctttctctccttcttcaaacttc) and *ROP6prom_R* (gtatagaaaagttgctaacaagctttcagaaaagaggatg) to give *ROP6prom/pDONRP4RP1*.

The ROP6 genomic sequence (*ROP6g – At4g35020*) from the ATG to its 3'UTR was amplified from *Col0* genomic DNA. Gateway compatible PCR products were introduced into *pDONRP2R-P3* (Thermofisher, www.thermofisher.com, cat# 12537023) vectors by BP recombination using the following primers: *ROP6-B2R (ggggacagctttcttgtacaaagtggctatgagtgcttcaaggtttatcaagtg)* and *ROP6-B3w3'UTR* (*ggggacaactttgtataataaagttgccttaagacaattggtgtgaatctagg*) to give *ROP6g/pDONRP2RP3*.

Mutation in *ROP6* were obtained by successive site directed mutagenesis using the following partially overlapping forward and reverse primers:
*ROP6-CA-fw* (*gtcggcgacgttgctgttggaaagacttgtc*) and *ROP6-CA-Rev* (*tccaacagcaacgtcgccgacagtgacacacttgataaacc*) using *ROP6g/pDONRP2RP3* as template to give *ROP6g-CA/pDONRP2RP3.*
Mutations in *ROP6g-PBR* were obtained by ligation using the following 5'-phosphorylated primers:
*ROP6g-7Q_F* (*gctgctgctggttttttggtggctggagaacgac*) and *ROP6g-7Q_R* (*agcagcaacaatctcagaaaggttgttctatactc*) using *ROP6g/pDONRP2RP3* as template to give *ROP6g$_{7Q}$/pDONRP2RP3.*
*ROP6g-3Q_F* (*ccaaaaaacaagcagaagcagaagcagaaatctcagaaaggttgttc*) and *ROP6g-3Q_R* (*gagatttctgcttctgcttctgcttgttttttggtggctggagaacgacc*) using *ROP6g/pDONRP2RP3* as template to give *ROP6g$_{3Q}$/pDONRP2RP3*.

The *ROP6* coding sequence (CDS) was amplified from *Col0* cDNA. Gateway compatible PCR products were introduced into *pDONRP221* (Thermofisher, www.thermofisher.com, cat# 12536017) vectors by BP recombination using the following primers: *ROP6-B1* (*ggggacaagtttgtacaaaaaagcaggcttaatgagtgcttcaaggtttatcaagtg*) and *ROP6-B2wSTOP* (*ggggaccactttgtacaagaaagctgggtatcagagtatagaacaacctttctgag*) to give *ROP6cDNA/pDONRP221*.
Mutations in *ROP6cDNA-PBR* were obtained by ligation using the *ROP6g-7Q_F* and *ROP6g-7Q_R* 5' phosphorylated primers and *ROP6cDNA/pDONRP221* as template to give *ROP6$_{7Q}$cDNA/pDONRP221*.

The *ROP6 C*-terminal tail, wild type and mutated ones were generated using the following 5' phosphorylated primers followed by a ligation:
*ROP6C-term_F* (*aaaatctcagaaaggttgttctatactctaagcaactttattatacaaagttggc*) and *ROP6Cterm_R* (*gctgctgctggttttttggagccactttgtacaagaaagttgaacg*) using *mCITRINE/pDONRP2RP3* as template to give *ROP6-C-term/pDONRP2RP3*.
*ROP6-3Q-C-term_F* (*agaaatctcagaaaggttgttctatactctaagcaactttattatacaaagttggc*) and *ROP6-3QCterm_R* (*gcttctgcttctgcttgttttttggagccactttgtacaagaaagttgaacg*) using *mCITRINE/pDONRP2RP3* as template to give *ROP6$_{3Q}$-C-term/pDONRP2RP3*.
*ROP6-7Q-C-term_F* (*agcagcaacaatctcagaaaggttgttctatactctaagc*) and *ROP6-7QCterm_R* (*gctgctgctggttttttggagccactttgtacaagaaagttgaacg*) using *mCITRINE/pDONRP2RP3* as template to give *ROP6$_{7Q}$-C-term/pDONRP2RP3*.

*mEos/pDONRP221* was obtained by amplifying *mEos* using the following primers: *mEOS_F* (*ggggacaagtttgtacaaaaaagcaggcttaatgagtgcgattaagccagacatgaag*) and *mEOS_R* (*ggggaccactttgtacaagaaagctgggtattatcgtctggcattgtcaggcaatc*) followed by BP cloning into *pDONRP221.*

The *PSS1* (*At1g15110*) coding sequence was amplified from *Col0* cDNA. Gateway compatible PCR products were introduced into *pDONRP221* vectors by BP recombination using the following primers: *PSS1-OX_F* (*ggggacaagtttgtacaaaaaagcaggcttaaccatggaacccaatgggtacaggaaa*) and *PSS1-OX_R* (*ggggaccactttgtacaagaaagctgggtaacgtctcttttgcgcgaggatcttct*) to give *PSS1cDNA/pDONRP221.*

*PSS1* artificial microRNAs were generated using WMD3-Web MicroRNA designer (Ossowski Stephan, Fitz Joffrey, Schwab Rebecca, Riester Markus and Weigel Detlef, personal communication). The *PSS1-AMI1_B1_B2* and *PSS1-AMI2_B1_B2* were produced by IDT to be introduced into *pDONRP221* vectors by BP recombination.

*PSS1-AMI1_B1_B2:*

*Acaagtttgtacaaaaaagcaggctcaaacacacgctcggacgcatattacacatgttcatacacttaatactcgctgttttgaattgatgttttag*
*gaatatatatgtaga**taataatgatgcgcttaacgt**tcacaggtcgtgatatgattcaattagcttccgactcattcatccaaataccgagtcgcca*
*aaattcaaactagactcgttaaatgaatgaatgatgcggtagacaaattggatcattgattctctttga**acgttaagcgcatcattatta**tctctct*
*tttgtattccaattttcttgattaatctttcctgcacaaaaacatgcttgatccactaagtgacatatatgctgccttcgtatatatagttctggta*
*aaattaacattttgggtttatctttatttaaggcatcgccatgacccagctttcttgtacaaagtggt*

*PSS1-AMI2_B1_B2:*

*acaagtttgtacaaaaaagcaggctcaaacacacgctcggacgcatattacacatgttcatacacttaatactcgctgttttgaattgatgttttag*
*gaatatatatgtaga**tttaacgtctctttttgcgcgc**tcacaggtcgtgatatgattcaattagcttccgactcattcatccaaataccgagtcgcca*
*aaattcaaactagactcgttaaatgaatgaatgatgcggtagacaaattggatcattgattctctttga**gcgcgcaaaagagacgttaaa**tctctct*
*tttgtattccaattttcttgattaatctttcctgcacaaaaacatgcttgatccactaagtgacatatatgctgccttcgtatatatagttctggta*
*aaattaacattttgggtttatctttatttaaggcatcgccatgacccagctttcttgtacaaagtggt*

The *RaichuROP6* constructs were based on Raichu-Rac1 and Raichu-Cdc42 constructs (*35*-*37*). In Raichu-Rac1/Cdc42 sensors, the CRIB domain of human PAK1 is cloned in tandem with Rac1 or Cdc42 (interspaced by an appropriate linker) and flanked by two fluorescent protein FRET pairs (Venus and ECFP) (*35*-*37*). The CRIB domain interacts specifically with activated Rac1/Cdc42 (i.e. GTP-bound Rac1 or Cdc42), which induces a conformational change in the sensor and enhances the FRET efficiency between the two fluorescent proteins. We used a similar design for the Raichu-ROP6 sensor. Because the CRIB domain of human PAK1 is known to also interact with plants GTP-bound ROPs (*12, 38*), we used this domain as a generic probe for ROP6-GTP conformation. To clone the *RaichuROP6* constructs, we first ordered a synthetic gene with the following sequence and flanked by *AttB1* and *AttB2* regions and subsequently cloned it into *pDONR221* by BP recombination:

*ggggacaagtttgtacaaaaaagcaggcttagaattcggcatggtatccaaaggtgaagaattatttacgggagtcgtgccaatacttgtcgagttg*
*gacggtgatgtgaacgggcataaattttcagtaagcggggagggagagggtgacgctacatacggaaaattaactttgaaactaatctgtaccacag*
*gaaaactgcctgtaccgtggcctactctcgtaacaacacttggttacggtttacaatgttttgcacgttaccccgaccatatgaaacaacatgacttt*
*cttcaaatctgcgatgcccgagggctatgttcaagaaaggactatattcttcaaggacgacggtaattacaaaactagagctgaagtcaagttcgaaa*
*ggagacacgctcgtgaataggatcgagttaaagggaatcgacttcaaagaagatggaaacattctgggacacaaattggagtacaactataattccc*
*ataacgtttacatcaccgccgacaaacaaaagaacgggataaaggcaaacttcaagattaggcacaatattgaggatgggggagtccagttagccga*
*tcactaccagcaaaatactcccataggtgacgggcccgtgctgcttcccgataatcattatctatcataccagtctgcgcttagcaaagaccctaac*
*gagaagagagatcacatggtcttgttggaattcgtaacagctgccctcgagaaagagaaagagcggccagagatttctctcccttcagattttgaac*
*acacaattcatgtcggttttgatgctgtcacaggggagtttacgggaatgccagagcagtgggcccgcttgcttcagacatcaaatatcactaagtc*
*ggagcagaagaaaaacccgcaggctgttctggatgtgttggagttttacaactcgaagaagacatccaacagccagaaatacatgagctttacagat*
*aagtcagcttccggaggtggaaccggtggtggaggtaccatgagtgcttcaaggtttatcaagtgtgtcactgtcggcgacggtgctgttggaaaga*
*cttgtcttctcatctcctacactagcaacactttccccacggattatgtgccaactgtgttcgataatttcagtgccaatgtgattgttgatggcaa*
*cactatcaacttgggattgtgggatactgcagggcaagaggactacaatagactaagacctttgagctatcgcggtgcagatgtcttcttacttgca*
*ttctcacttgtcagcaaagctagctatgaaaatgtttctaaaaagtgggttcctgaactgagacattatgctcctggtgttcccatcatcctcgttg*
*gaacaaagcttgatcttcgagatgataagcaattctttgccgagcaccctggtgctgtgcctatctctaccgctcagggtgaagaactaaagaagct*
*gattggggcgcctgcttatatcgaatgcagtgcaaaaactcaacagaatgtgaaagcagtgtttgatgcggctatcaaggtcgttcgcggccgcatg*
*gtgtccaagggagaagaacttttaccggagtagtacctatacttgtcgagctcgatggggatgtcaatggtcaccgtttctcagtcagcggggaag*
*gcgagggtgacgcgacttacgggaaattaaccctaaaatttatatgcaccacgggaaagctgccagtaccctggcccaccctggtcaccaccctaac*
*ctggggcgtccagtgtttctcacgataccctgaccacatgaagcaacacgatttcttcaaatcagctatgcccgaggggtatgtccaggagagaacg*
*atatttttaaggatgatgggaattacaagactagggctgaggttaagttcgaaggggatacgcttgtgaacaggatagagttaaaaggcattggct*
*ttaaggaggatggtaacatccttggccacaaactagagtataactacatcagtcataacgtgtacataacggccgataagcagaagaatggtattaa*
*ggcacattttaagataagacacaacatcgaagatggtggggtccaactggctgatcattaccagcaaaatactcctatcggcgacggccctgtattg*
*ctaccggacaatcactacctaagtactcaaagcgcgttatccaaggaccctaacgagaagagagatcacatggttctgcttgaatttgtgaccgcag*
*ctggaatcacgcttggaatggacgaactgtctagagtcgctatcaaggtcgttctccagccaccaaaaaacaagaagaagaagaagagaaaatctca*
*gaaaggttgttctatactctagggatcctacccagctttcttgtacaaagtggtcccc*

*RaichuROP6/pDONR221* was then used as template for PCR amplification by the *ROP6-CA_F* and *ROP6-CA_R* primers to give *RaichuROP6$_{CA}$/pDONR221*.
*RaichuROP6$_{CA}$/pDONR221* was then used as template for PCR amplification by the 5' phosphorylated *RaichuROP6-7Q_F* (*caacaatctcagaaaggttgttctatactctagggatcctacccagctttcttgtac*) and *RaichuROP6-7Q_R* (*ctgctgctgctgctggtttttggtggctggagaacgaccttgatagcgactctagac*) primers followed by ligation to give *RaichuROP6$_{CA\text{-}7Q}$/pDONR221*.

Cloning: construction of destination clones (destination vector).
The following gateway entry vectors were previously published: *pTNT-HA-ccdb (20); UBQ10prom/pDONR P4P1R (NASC# N2106315) (39), 2x35sprom/pDONR P4P1R (NASC# N2106316) (39), mCITRINEnoSTOP/pDONR221 (NASC# N2106287) (40);* and *2xPH$_{EVCT2}$/pDONR P2RP3 (10).*
Binary destination vectors for plant transformation were obtained using the multisite LR recombination system (life technologies, http://www.thermofisher.com/) using the *pB7m34GW* (basta resistant) or *pK7m34GW* (Kanamycin resistant) *(41)* as destination vectors, and the donor vectors describe above to give:
*pROP6prom::mCITRINE-ROP6/pB7m34GW, pROP6prom::mCITRINE-ROP6$_{3Q}$/pB7m34GW, pROP6prom::mCITRINE-ROP6$_{7Q}$/pB7m34GW, 2x35sprom::mEOS-ROP6/pB7m34GW, 2x35sprom::mEOS-ROP6$_{7Q}$/pB7m34GW, 2x35sprom::mEOS-ROP6$_{CA}$/pB7m34GW, UBQ10prom::mCITRINE-ROP6$_{C\text{-}term}$/pB7m34GW, UBQ10prom::mCITRINE-ROP6$_{3Q\text{-}C\text{-}term}$/pB7m34GW, UBQ10prom::mCITRINE-ROP6$_{7Q\text{-}C\text{-}term}$/pB7m34GW, 2x35sprom::mEOS-2xPH$_{EVCT2}$/pB7m34GW, promUBQ10::PSS1cDNA-mCITRINE/pB7m34GW (PSS1-OX), promUBQ10::PSS1-AMI1/pK7m34GW (PSS1-AMI1), promUBQ10::PSS1-AMI2/pK7m34GW (PSS1-AMI2), prom2x35S::RaichuROP6/pB7m34GW, prom2x35S::RaichuROP6$_{CA}$/pB7m34GW, prom2x35S::RaichuROP6$_{CA\text{-}7Q}$/pB7m34GW.*
Transgenic lines were obtained as described in (*39*).

Each transgenic line was used as follow:
***UBQ10prom::mCitrine-C2$_{LACT}$*** *(20):* Fig. 1A and B, Fig. S1F.
***UBQ10prom::mCitrine-2xPH$_{EVCT2}$*** *(10):* Fig. S1B and C, Fig S1F.
***UBQ10prom::Lti6b-2xmCHERRY*** (*26*): Fig. S1D and F.
***UBQ10prom::mCitrine-2xPH$_{FAPP1}$*** *(25):* Fig. S1D.
***UBQ10prom::mCitrine-P4M*** *(20):* Fig. S1D and E.
***UBQ10prom::mCitrine-2xPH$_{PLC}$*** *(25):* Fig. S1D.
***UBQ10prom::mCitrine-TUBBYC*** *(25):* Fig. S1D.
***UBQ10prom::mCitrine-1xPASS*** *(10):* Fig. S1D and E.
***UBQ10prom::mCitrine-KA1$_{MARK1}$*** *(20):* Fig. S1D and E.
***pss1-3xUBQ10prom::Lti6b-2xmCHERRY****(25):* Fig. S1D and F.
***pss1-3xUBQ10prom::mCitrine-2xPH$_{FAPP1}$*** *(25):* Fig. S1D.
***pss1-3xUBQ10prom::mCitrine-P4M*** *(25):* Fig. S1D and E.
***pss1-3xUBQ10prom::mCitrine-2xPH$_{PLC}$*** *(25):* Fig. S1D.
***pss1-3xUBQ10prom::mCitrine-TUBBYC*** *(25):* Fig. S1D.
***pss1-3xUBQ10prom::mCitrine-1xPASS*** *(10):* Fig. S1D and E.
***pss1-3xUBQ10prom::mCitrine-KA1$_{MARK1}$*** *(10):* Fig. S1D and E.
***pss1-3*** (*10*): Fig. 2A and C, Fig. 4A-C and E, Fig. 5F, Fig. S1D and E, Fig. S3A and B, Fig. S4A-F and I, Fig. S5A-B, Fig. S7A-B, D, E and F, Fig. S10E, Fig. S16C and D, Fig. S17B-F.

***pss1-4*** (*10*): Fig. S3B, Fig. S17B-F.
***pss1-5*** (*10*): Fig. S3B, Fig. S17B-E.
***pss1-3xpPSS1::PSS1g*** *(pss1-3xPSS1prom::PSS1genomic)* (*10*): Fig. 2A, Fig. S4A, Fig. S17C and D.
***GFP-ROP6*** *(2x35S::GFP-ROP6)* (*22*): Fig. 3A-B, Fig. 4A, B and E, Fig. S5A-B, Fig. S7A-C, E and F, Fig. S8A-B, Fig. S13D, Fig. S17C and D.
***pss1-3xGFP-ROP6***: Fig. 4A, C and E, Fig. S5A and B, Fig. S7A, B, E-F
***UBQ10prom::2xmCherry-C2$_{LACT}$x2x35S::GFP-ROP6****:* Fig. 5C
***GFP-ROP6$_{CA}$*** *(2x35S::GFP-ROP6-CA) (22):* Fig. S17C and D.
***PSS1-OX*** *(UBQ10prom::PSS1-mCitrine):* Fig. 2B and D, Fig. S2A-B, Fig. S4G-I.
***PSS1-AMI*** *(UBQ10prom::AMI1 and UBQ10prom::AMI2):* Fig. 2B and D, Fig. S2A-B, Fig. S4G-I.
***CLC2-GFP*** *(pCLC2::CLC2-GFP) (27)* and ***pss1-3xCLC2-GFP****:* Fig. S4E.
***GFP-TUA6*** *(35S::GFP-TUA6, NASC #6551)* and ***pss1-3xTUA6-GFP***: Fig. S4F.
***mEos-ROP6*** *(also called* ***ROP6-OX*** *for phenotypic analyses, 2x35prom::mEos-ROP6)*: Fig. 2A, Fig. 3C-F, Fig. 5D and E, Fig. S9B-F, Fig. S10B-C and E, Fig. S14D-F.
***pss1-3xmEos-ROP6*** *(also called* ***pss1-3xROP6-OX*** *for phenotypic analyses)*: Fig. 2A, Fig. 5F, Fig. S10E, Fig. S16C and D.
***mEos-ROP6$_{CA}$*** *(also called* ***ROP6$_{CA}$*** *for phenotypic analyses, 2x35S::mEos-ROP6$_{CA}$):* Fig. 2A and C, Fig. 3D and F, Fig. 4D, Fig. S9A, Fig. S10A and E, Fig. S11A and C.
***mEos-ROP6$_{CA}$xpss1-3****:* Fig. 2A and C
***mEos-ROP6$_{CA}$xPSS1-OX****:* Fig. 4D, Fig. S11B and C.
***mEos-ROP6$_{7Q}$*** *(also called* ***ROP6$_{7Q}$-OX*** *for phenotypic analyses,2x35S::mEos-ROP6$_{7Q}$):* Fig. 5D-F, Fig. S14D-F, Fig. S16A and B.
**mEos-2xPH$_{EVCT2}$** (2x35S::mEos-2xPH$_{EVCT2}$): Fig. 5A and B, Fig. S12A-C.
***rop6-2*** *(16)*: Fig. S14B and C, Fig. S17C and D.
***PIN2-GFP*** *(28) (pPIN2::PIN2-GFP)* and ***pss1-3xPIN2-GFP***: Fig. S4B-D.
***rop6-2xPIN2-GFP***: Fig. S4B-C.
***rop6-2xROP6prom::mCitrine-ROP6***: Fig. S13C and D, Fig. S14A-C.
***rop6-2xROP6prom::mCitrine-ROP6$_{3Q}$***: Fig. S13C.
***rop6-2xROP6prom::mCitrine-ROP6$_{7Q}$***: Fig. S13C and Fig. S14A-C.
***UBQ10prom::mCitrine-ROP6-C-term****:* Fig. S13C and D.
***UBQ10prom::mCitrine-ROP6$_{3Q}$-C-term****:* Fig. S13C.
***UBQ10prom::mCitrine-ROP6$_{7Q}$-C-term****:* Fig. S13C.
***PIP2a-mEos*** *(pUBQ10::PIP2a-mEOS) (29):* Fig. S14F.

Recombinant protein expression and lipid-protein overlay assays.
The expression plasmids *pTNT::HA-ROP6cDNA* and *pTNT::HA-ROP6$_{7Q}$cDNA* were obtained by LR recombination between *ROP6cDNA/pDONR221*, *ROP6$_{7Q}$cDNA/pDONR221* entry vectors and the *pTNT-HA-ccdb* destination vector (*42*). The expression plasmids *pTNT::HA-ROP6cDNA* and *pTNT::HA-ROP6$_{7Q}$cDNA* were used as DNA template for *in vitro* transcription and translation using the TNT® SP6 High-Yield Wheat Germ Protein Expression System (Promega, www.promega.com), following manufacturer's instructions. 5µl of the total reaction were used to analyze protein expression levels by western-blot using 1:1000 anti-HA (www.boehringer-ingelheim.com) primary antibody and 1:5000 secondary anti-mouse (GE Healthcare Life Sciences, http://www.gelifesciences.com/) antibody. The lipid overlay assays were performed as follow:

nitrocellulose membranes containing immobilized purified lipids (PIPstrip P-6001, Echelon Bioscience, http://echelon-inc.com/) were incubated for 60 min in blocking solution (TBST (50 mM Tris, 150 mM NaCl, 0,05% Tween 20, pH 7.6) + 3% BSA). Membranes were then incubated for 2h with 10mL of blocking solution containing 40 µl of in vitro synthesized proteins. After three washing steps using blocking solution, membranes were incubated for 120 min at room temperature with primary antibodies diluted in blocking solution, rinsed three times with blocking solution and incubated for 60 min at room temperature with the secondary antibody also diluted in blocking solution. Antibodies and dilutions are the same as described above.

Recombinant protein expression and purification for enzymology assay.

The full length *ROP6* WT and *ROP6*$^{7Q}$ coding sequences were inserted in pET28a+ between NdeI and NotI for overexpression in Escherichia coli (DE3) Rosetta pLysS (Novagen, www.merckmillipore.com/). The bacterial culture (2xTY medium, www.sigmaaldrich.com) from overnight preculture was incubated at 37°C. The induction was performed at OD 0.55 with 0.5mM IPTG + 5% glycerol and incubated at 18°C overnight. The cells were pelleted, resuspended in 20mM Tris, 400mM NaCl, 5mM beta-mercaptoethanol and flash frozen. After thawing, the cells were lysed by sonication and centrifuged at 15,000g for 35 minutes at 4°C. The supernatant was applied on a Nickel Immobilized Metal ion Affinity Chromatography at room temperature. The beads were washed with 10 volumes of 20mM Tris, 400mM NaCl, 20mM imidazole and then with 5 volumes of 20mM Tris, 400mM NaCl, 60mM imidazole. The beads were then eluted with 20mM Tris, 150mM NaCl, 0.4M imidazole. The elution fraction was centrifuged at 20,000g for 20 minutes at 4°C before purification by the Size Exclusion Chromatography (SEC) column Superdex 75 16/60 in 20mM Tris, NaCl 150mM pH 8 at 1mL/min. The fractions corresponding to ROP6 both pure and non-aggregated are pooled and concentrated at 50 µM.

GTPase assay.

The ROP6 proteins used for the assays were never frozen and used less than 24 hours after their purification. GTP hydrolysis was detected using Biomol Green (Enzo lifescience, www.enzolifesciences.com/) following the 1mL sample commercial protocol. The concentrations used for the reactions were 80µM GTP, 10µM ROP6, 10µM BSA in 20mM Tris, NaCl 150mM, 2mM MgCl2 pH 8. The GTPase reactions were incubated at 22°C for 75 minutes. The measures were repeated three time, with independent ROP6 purification and independent phosphate calibration for each set of experiments.

Western blot.

20µl of the total reaction were used to analyze protein expression levels by western-blot using 1:2000 anti-Eos (A010-mEOS2, https://badrilla.com) and 1:10000 anti H3 (www.boehringer-ingelheim.com) primary antibodies incubated overnight at 4°C. 1:5000 secondary anti-rabbit-HRP antibody was applied at room temperature for 60 min (www.thermofisher.com). For revelation, ECL prime was applied for 30 seconds.

qRT-PCR.

Total RNA was extracted using the Spectrum Plant Total RNA Kit (Sigma). Total RNAs were digested with Turbo DNA-free DNase I (Ambion) according to the manufacturer's instructions. RNA was reverse transcribed using the SuperScript VILO cDNA Synthesis Kit (Invitrogen) according to the manufacturer's protocol. PCR reactions were performed in an optical 396-well

plate in the QuantStudio 6 Flex Real-Time PCR System (Applied Biosystems), using FastStart Universal SYBR Green Master (Rox) (Roche), in a final volume of 10 µl, according to the manufacturer's instructions. The following standard thermal profile was used for all PCR reactions: 95 °C for 10 min, 40 cycles of 95 °C for 10 s, and 60 °C for 30 s. Data were analyzed using the QuantStudio 6 Flex Real-Time PCR System Software (Applied Biosystems; www.thermofisher.com).

Two set of primers were used to amplify *PSS1* cDNA, the first set of primers (black dots on Fig. S1D) *ggcttacaagcctcgcactatc*/*tcaagagctccactagcccaaatg* was located at the *5'* end of *PSS1* cDNA. The second set of primers (grey dots on Fig. S1D) *gcattctgttggctgtcactgg*/*ttctgttgggtacaatccacttcc* was located at the *3'* end of the *PSS1* cDNA. As a reference, the primers *gactacagtccactcaatcactgc/aagagctggaagcacctttccg* were used to amplify the *GAPC1* (At3g04120) cDNA. PCR efficiency (*E*) was estimated from the data obtained from standard curve amplification using the equation $E=10^{-1/slope}$. Expression levels are presented as $E^{-CtPSS1}$ / $E^{-CtGAPC1}$.

Lipid extraction.

12 days old seedlings (0.1-1g fresh weight) were collected in glass tubes; 2 ml of preheated isopropanol were added and tubes were heated at 70°C for 20 min to inhibit phospholipase D activity. 6 ml of chloroform/methanol 2/1 (v/v) were added and lipid extraction was completed at room temperature. The organic phases were transferred to new glass tubes. Then 1.5 ml of H2O was added to the organic phases and tubes were vortexed and centrifuged at 2000rpm; the organic phases were transferred to new glass tubes, evaporated and the lipids were resuspended in the appropriate volume of chloroform/methanol 2/1, v/v, in order to obtain the same concentration according to the initial seedlings fresh weight.

Lipid quantification by high performance thin layer chromatography (HPTLC).

Lipids were deposited on HPTLC plates (Silica gel 60G F254 glass plates Merck Millipore) together with external pure lipid standards (Avanti lipids). Plates were developed according to (*43*). Following chromatography, the lipids were charred for densitometry according to (*44*). Briefly, plates were dipped into a 3% cupric acetate (w/v)-8% orthophosphoric acid (v/v) solution in H2O and heated at 110°C for 30min. Plates were scanned at 366 nm using a CAMAG TLC scanner 3. 6 independent samples were quantified for wild type, *PSS1-AMI1*, *PSS1-AMI2*, *PSS1-OX1* and *PSS1-OX2* plants.

## IMAGE QUANTIFICATIONS:

Gravitropic response and gravitropic defects.

7-8 days old seedlings were subjected to 135° angle for 12 hours. For each genotype analyzed at least 30 roots in three independent experiments were used for quantification. Every 4 hours, plates were scanned with EPSON scanner perfection V300 PHOTO at 800 dpi. Each plate at the different time points were cropped and aligned using "Template Matching and Slice Alignment" plugin on FIJI(*45*) (https://fiji.sc/) to obtain a timelapse for 12h. To allow high throughput data analyses, the process has been automatized on a macro. To quantify the average root angle of curvature RootTrace software was used (*46*). In Fig. 2A, 2B and 5D, statistical analyses were performed on the root bending at 8 hours after reorientation.

The horizontal and vertical growth index were calculated on 10-day-old wild-type, *pss1-3*, *pss1-4* and *pss1-5* seedlings using the "segment line" tool on FIJI. Briefly, to calculate the gravitropic indexes, three length are considered, L, $L_y$ and $L_x$ (*47*). L is the total length of the roots (from base of hypocotyl to root tip), while $L_y$ and $L_x$ are, respectively, ordinate and abscissa of the root tip (considered from the point of view of the base of hypocotyl). The horizontal growth index (HGI) corresponds to the ratio $L_x/L$, while the vertical growth index (VGI) corresponds to the ratio $L_y/L$ (*47*). For WT and *pss1-3* at least 44 roots in three independent experiments were used and one experiment for *pss1-4* and *pss1-5*. In each graph relative to gravitropic response and defect, "n" represents the number of roots used for quantification.

Size of FM4-64-stained BFA bodies.

BFA body size was quantified on at least 14 roots representing an average of 602 cells in three independent experiments. Threshold was applied, images harboring less than ten BFA bodies were removed from the analysis as well as images issue from misshapen root cells. Cells containing BFA bodies whose length are bigger than width were selected for the analysis. Images were submitted to a NidBlack auto local threshold with a radius of 15. BFA bodies bigger than 5.2 $um^2$ with a circularity between 0.25 and 1 were detected using the "Analyze Particles" plugin of FIJI. The average size of BFA bodies was obtain for one root. Per root an average of 38 BFA bodies was detected representing at least 532 BFA bodies quantified per conditions. All this process has been automatized using a macro. In each graph relative to the size of BFA body, "n" represents the number of roots used for quantification

Number of PIN2-GFP BFA-body per cells.

10- to 12-day-old seedlings expressing PIN2-GFP in WT, *rop6-2* and *pss1-3* were used to quantify the number of cells containing PIN2 BFA bodies. At least 6 roots representing 265 cells in one experiment were used for quantification (Fig. S4). For the concomitant treatment of BFA and NAA in Fig. S2, for WT and *pss1-3* at least 29 roots representing 1734 cells in three independent experiment (except for *rop6-2* one experiment) were used for quantification. The percentage of cell was obtained counting by eyes the number of PIN2 BFA divided by the number of cells in the root meristematic and elongation zones multiplied by one hundred. In each graph relative to the number of PIN2-GFP BFA-bodies per cell, "n" represents the number of roots used for quantification.

Percentage of CLC2-GFP at plasma membrane (PM).

Plasma membrane-positive CLC2-GFP were counted by eyes on at least 21 roots of 10-to 12-day-old seedlings, representing 698 cells in three independent experiments. The percentage of cells with CLC2 at the plasma membrane was obtained counting the number of plasma membrane-positive CLC2 divided by the number of cells in the root meristematic zone multiplied by one hundred. In the graph relative to the percentage of CLC2-GFP at the plasma membrane, "n" represents the number of roots used for quantification.

Microtubules orientation.

Microtubule arrays were acquired on 10- to 12-day-old seedlings in the elongation zone of root cells. The average orientation was calculated on at least 28 cells of 13 roots in two independent experiments using FibrilTool plugin (*48*) on Fiji (*45*). In the graph relative to microtubule orientation, "n" represents the number of cells used for quantification.

Number of spots per cell.

The number of spots per cells was calculated using SiCESpotDetector.ijm plugin (*49*) (http://www.enslyon.fr/RDP/SiCE/METHODS_files/SiCE%20SpotDetectorV3.ijm) on 5 to 7-day old transgenic plants expressing ROP6, ROP6$_{3Q}$, ROP6$_{7Q}$ full length fused to mCITRINE expressed by its own promoter or the ROP6 C-terminal wild-type, 3Q and 7Q fused to mCITRINE expressed under the *UBQ10prom*. The quantifications were made on at least 12 roots representing an average of 516 cells. In the graph relative to the number of spots per cell, "n" represents the number of roots used for quantification.

Fluorescence intensity at plasma membrane.

5- to 7-day old transgenic lines were used to quantified the plasma membrane intensity according to the integrated density tool of ImageJ (*32*). The integrated density at the plasma membrane in the basal meristem was average from 60 cells taken from three independent roots using a three-pixel line width and the "Measure" tool in Fiji. Note that we used the integrated density as read out to evaluate the fluorescence intensity to directly normalize the intensity according to the size of the ROI. In graphs relative to the fluorescence intensity at the plasma membrane, "n" represents the number of cells used for quantification.

SptPALM data quantifications and representations.

For each movie corresponding to one condition/genotype, the natural logarithm of apparent diffusion coefficient (log(D)) per molecule was extracted from MTT data (*33*) by CBS sptPALM analyzer (*34*). For sptPALM analyses, only tracks with at least five successive points were selected and the rest of the molecules were discarded from the analysis. We pooled values from each condition in order to get the log(D) distribution using R software (as histogram shown on left panel of Fig. S9, S11, S12 and S16, number of bins set to 80). A first partition P was done; the set of molecules which present a log(D) value below -1.75 refers to the immobile group, whereas values above this threshold denote the mobile group. To obtain the percentage of molecules in the immobile group, we divided the number of tracks below -1.75 by the total track number multiplied by one hundred. Then, each condition was analyzed using an R script to automatize the analysis. To statistically test the existence of these two behaviors (mobile and immobile), we analyzed the log(D) distribution per condition using the mclust R package. For each condition, the percentages of data in each of the 2 groups defined by the partition P with the absolute log(D) value (-1.75) are first reported. We then fitted two distinct two-component Gaussian mixture models, M0 and M1, using the mclust::Mclust R function. M0 is a model where $\sigma_1 \neq \sigma_2$ and M1 is a model where $\sigma_1 = \sigma_2$. For each model, every molecule is assigned to one of the 2 Gaussian components $G_i$ ($i \in [1, 2]$) according to a MAP (Maximum A Posteriori)-based classification. M1 model was used since it provided more representative results despite of a lower Bayesian information criterion values. The percentage of values assigned to each of the two Gaussian components is reported as well as its 95% confidence interval obtained with a non-parametric bootstrap method, using the mclust::MclustBootstrap R function with default arguments. The classification rate was calculated as the percentage of MAP-classified values concordant with the partition P. Based on the estimation of the model M1, we plotted the density of the Gaussian mixture according to the kernel density estimation (called "occurrence" for more clarity) and used for representation (as Fig. S9, S11, S12 and S16, right panel). At least 14 acquisitions from three independent experiments were used, representing 12,824 tracks. In each graph relative to the percentage of immobile ROP6, "n"

represents the number of acquisitions used for quantification. Note that one acquisition may represent more than one cell but that different acquisitions are always from different cells.

LivePALM, Voronoi tessellation analyses and representation.

For each movie corresponding to one condition/genotype, the object localization was extracted from MTT data (*33*) by CBS sptPALM analyzer (*34*). SR-tesseler software was used to reconstruct live PALM images and determine protein local density (*50*). Multiple detections of single object were corrected as previously described by Levet et al. (*50*). Local density was extracted from Voronoï segmentation of the image as shown in Fig. 3E, 5A and Fig. S10. We pooled values from each condition in order to get the log(local density) distribution using R software (as histogram in Fig. S10, left panel, number of bins set to 80). A first partition P was done; the set of molecules which present a log(local density) value below 3.5 refers to the immobile group, whereas values above this threshold denote the mobile group. To obtain the percentage of molecules in the immobile group, we divided the number of molecules below 3.5 by the total molecules number multiplied by one hundred. Then, each condition was analyzed using an R script to automatize the analysis. To statistically test the existence of these two behaviors (mobile and immobile), we analyzed the local density distribution per condition using the mclust R package. For each condition, the percentages of data in each of the 2 groups defined by the partition P with the absolute log(local density) value (3.5) are first reported. We then fitted two distinct two-component Gaussian mixture models, M0 and M1, using the mclust::Mclust R function. M0 is a model where $\sigma_1 \neq \sigma_2$ and M1 is a model where $\sigma_1 = \sigma_2$. For each model, every molecule is assigned to one of the 2 Gaussian components $G_i$ ($i \in [1, 2]$) according to a MAP (Maximum A Posteriori)-based classification. M1 model was used since it provided more representative results despite of a lower Bayesian information criterion values. The percentage of values assigned to each of the two Gaussian components is reported as well as its 95% confidence interval obtained with a non-parametric bootstrap method, using the mclust::MclustBootstrap R function with default arguments. The classification rate was calculated as the percentage of MAP-classified values concordant with the partition P. Based on the estimation of the model M1, we plotted the density of the Gaussian mixture according to the kernel density estimation (called "occurrence" for more clarity) and used for representation (as Fig. S10, right panel). At least 24 cells from three independent experiments were used representing 1,319,164 molecules. In each graph relative to the fraction of clustered ROP6 in percentage, "n" represents the number of roots used for quantification.

Clusters density and size analysis.

For each movie corresponding to one condition/genotype, the local density of each molecule was calculated with SR-Tesseler (*50*). For cluster detection, a threshold of 20 times the average localization density was applied to identify regions with high local density. "Objects" with at least 5 molecules were identified as "clusters" of molecules (as shown in Fig. S10D) and from which the size of each cluster was extracted (as shown in Fig. S10E). n indicates the number of detected clusters.

GFP-ROP6 domain density.

An ImageJ macro was written to manually define homogenous area in plasma membrane on TIRF images. ROP6 microdomains were then manually selected using the multipoint tool of ImageJ and added to a result table with corresponding computed domain density. Cell position in Arabidopsis

root (basal meristem of elongation zone) was systematically registered after ROI selection for further analysis. In each graph relative to GFP-ROP6 domain density, "n" represents the number of regions of interest (ROI) used for quantification.

For the quantification of domain recovery after photobleaching (Fig. 4E), the total number of bleached GFP-ROP6 nanodomains were manually counted as well as the number of GFP-ROP6 nanodomains that recovered fluorescence. "n" represents the number of nanodomains that were present in the bleached region of interest.

Ratio PM/cytosol quantification.

To quantify the plasma membrane/cytosol ratio on phosphatidylserine biosensors mCITRINE-C2$_{LACT}$ and mCITRINE-2xPH$_{EVCT2}$, PI4P biosensor mCITRINE-P4M, PA biosensor mCITRINE-1xPASS, and membrane surface charge biosensor mCITRINE-KA1$_{MARK1}$, we calculated and analyzed the "Ratio plasma membrane/cytosol fluorescence intensity". This correspond to the ratio between the fluorescence intensity (Mean Grey Value function of Fiji software) measured in two elliptical region of interest (ROIs) from the plasma membrane region (one at the apical/basal plasma membrane region and one in the lateral plasma membrane region) and two elliptical ROIs in the cytosol. For mCITRINE-C2$_{LACT}$ and mCITRINE-2xPH$_{EVCT2}$, we quantified in 150 cells over three independent replicates (50 cells per replicate) for mock and NAA and 150 cells over two replicates for basal meristem and elongation zone. Note that for the ratio calculated in Fig. S1E for PA biosensor (mCITRINE-1xPASS) one replicate was used otherwise three replicates were used for the quantification of the membrane surface charge biosensor mCITRINE-KA1$_{MARK1}$ and PI4P biosensor mCITRINE-P4M (the number of cells is indicated on the figure). In each graph relative to the plasma membrane/cytosol ratio, "n" represents the number of cells used for quantification on at least 9 roots and on at least 17 roots in treated conditions.

Total fluorescent intensity.

To quantify the total fluorescence intensity in the basal meristem (BM) and in the elongation zone (EZ) for Lti6b-2xmCHERRY and the phosphatidylserine biosensors mCITRINE-C2$_{LACT}$ and mCITRINE-2xPH$_{EVCT2}$ the mean gray value of imageJ was used in the corresponding zone (BM or EZ) by drawing a region of interest (ROI) of 1900µm$_2$. The ROI represents approximately the width of three cell files. Note that we always used the same size of ROI which allowed us to directly compare the fluorescence intensity without normalization according to the size of the ROI. In each graph relative to the quantification of the total fluorescence, "n" represents the number of roots used for quantification on at least two independent replicates representing at least 18 roots.

Ratiometric FRET measurement.

The interaction between ROP6 and PAK-CRIB domains within the raichu sensors were evaluated by FRET calculation from the CFP to YFP. In each field of view, two pictures were recorded. The first corresponds to the CFP channel and give the donor fluorescence (Ex458, Em467-493). Whereas the second one is the FRET channel called YFP$_{FRET}$ (Ex458, Em 538-573). The ratio image, YFP$_{FRET}$/CFP, was calculated with Fiji software. Mean Grey value of each cells present in the field of view was measured independently by drawing specific ROI. At least 10 fields of view out of two independent transformation assays were analyzed. In graph relative to FRET measurements, "n" represents the number cells used for quantification.

Pavement cell circularity.

Stage 3 leaves of 28-day-old plants were used for pavement cell circularity quantification. For image acquisition, adaxial leaf epidermis were printed on tepid agar at 3% poured on a coverslip. 5 days after printing, pavement cell edges were observed on the slip using Zeiss IMAGER M5 AXIO optical microscope with 40x/0.75 Zeiss EZ. plan- NEOFLUAR objective with DIC illumination. At least 79 pavement cells of 5 independent leaves were analyzed with Fiji using the circularity measurement. In the graph relative to the pavement cell circularity, "n" represents the number of pavement cells used for quantification.

Root hair phenotype and initiation site ratio.

Root hair phenotyping and initiation site were observed on 5-day-old seedlings on at least 7 plants representing 336 root hairs for phenotyping and 48 for initiation site in two independent experiments. In order to determine the initiation site ratio, the length of the root hair initiation (l) from the basal side divided by the total length of the trichoblast (L) were measured. For image acquisition, plants were set up between glass and coverslip containing water and observed using Zeiss IMAGER M5 AXIO optical microscope with 40x/0.75 Zeiss EZ.plan-NEOFLUAR objective. In each graph relative to root hair phenotyping and initiation site, "n" represents the number of root hair cells used for quantification.

Lateral root density.

12-day-old seedlings were used for quantification for the complementation assay, plates were scanned with EPSON scanner perfection V300 PHOTO at 800 dpi. A ratio of the number of lateral roots divided by the root length was applied in order to calculate the lateral root density. At least 116 plants were analyzed in two independent experiments. In the graph relative to the lateral root density, "n" represents the number of roots used for quantification.

Statistical analyses.

Each sample were subjected to four different normality tests (Jarque-Bera, Lilliefors, Anderson-Darling and Shapiro-Wilk), sample were considered as a Gaussian distribution when at least one test was significant (p=0.05). Consequently, parametric or non-parametric test were performed. For parametric test, an ANOVA was performed coupled to a Fisher or Tukey test in order to proceed to pairwise comparison between samples (confidence index, 95%). Statistical analyses between two samples were performed using the Student t-test (p-value=0.05). For non-parametric test, results were statistically compared using the Kruskal-Wallis bilateral test (p-value=0.05 or 0.15 for gravitropism experiment) using XLstat software (http://www.xlstat.com/). Pairwise comparisons between groups were performed according to Steel-Dwass-Critchlow-Fligner or Conover-Iman procedure (different letters indicate statistical difference between samples) (Hollander and Wolfe, 1999). Statistical analyses between two samples were performed using the non-parametric Wilcoxon-Mann-Whitney test (p-value=0.05).

The following tests were performed for each graph in the main Figures and Supplementary Figures:

**Non-parametric test**:

Kruskal Wallis bilateral test combined with a multiple pairwise comparisons:

- Using the Conover-Iman procedure / Two-tailed test, significance level 15%: Fig. 2A
- Using the Steel-Dwass-Critchlow-Fligner, significance level 5%: Fig. 3F, Fig. 4B-C and E, Fig.S1E, Fig. S4E, Fig. S14C, Fig. S17C.

Wilcoxon-Mann-Whitney /Two-tailed test, significance level 5%: Fig. 1A-B, Fig. 3B, Fig. S1B-C and F, Fig. S7F, Fig S8A.

**Parametric test**:

Student t-test for two independent samples / Two-tailed test, significance level 5%: Fig. 3A and Fig. S8B, Fig. S9F, Fig. S11C an1 Fig. S12.

Two ways ANOVA, confidence index 95% combine with an analysis of the differences between the categories:

- Using the Fisher test: Fig. 2B-C, Fig. 3D, Fig. 4A, Fig. 5E-F, Fig S1A, Fig. S2A-B, Fig. S4C-D, F and H
- Using the Tukey test: Fig. 2D, Fig. 5D, Fig. S4A (85%), Fig. S13C, Fig. S14B, S15E

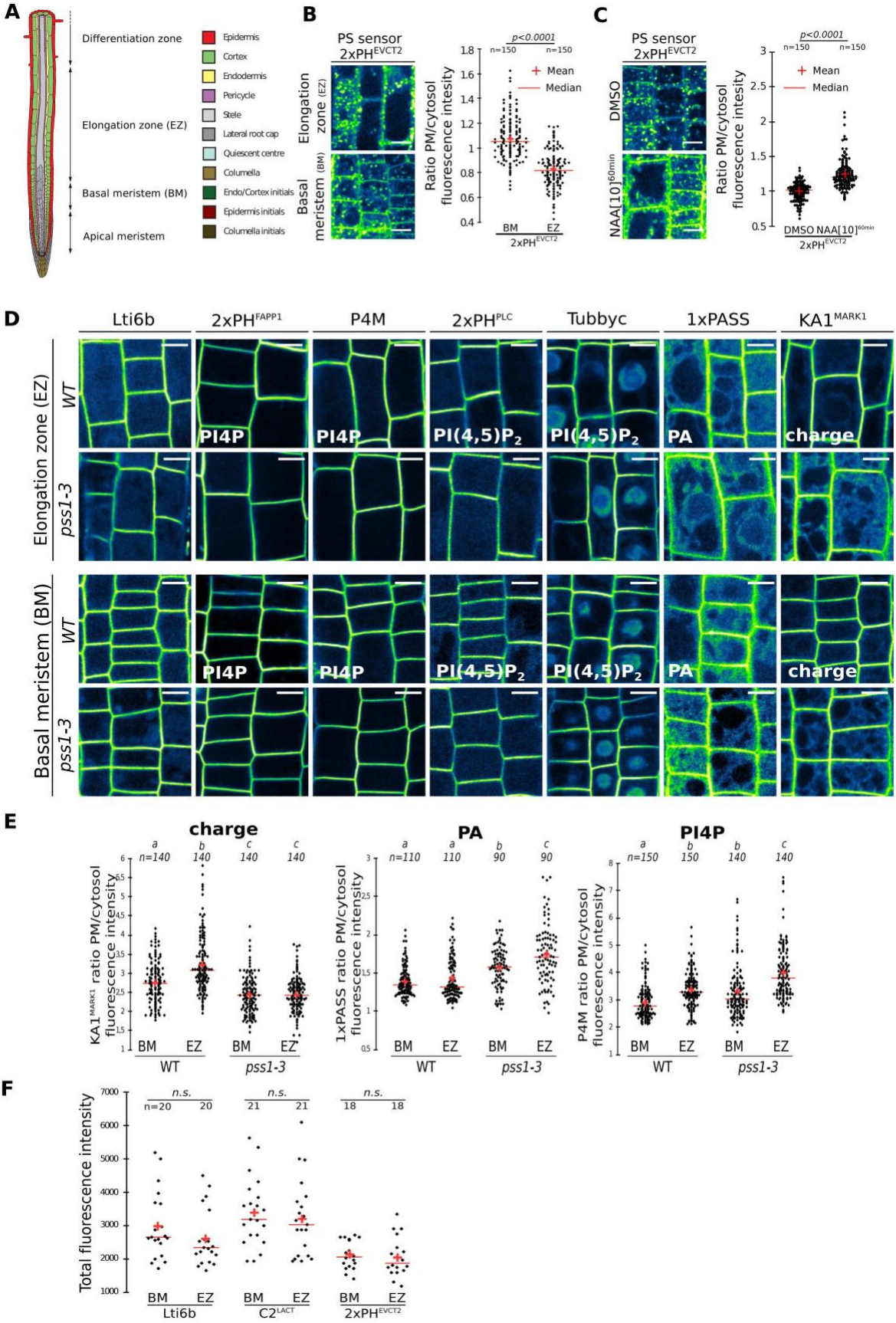
A
Differentiation zone
Elongation zone (EZ)
Basal meristem (BM)
Apical meristem
Epidermis
Cortex
Endodermis
Pericycle
Stele
Lateral root cap
Quiescent centre
Columella
Endo/Cortex initials
Epidermis initials
Columella initials
B
PS sensor 2xPH^EVCT2
Elongation zone (EZ)
Basal meristem (BM)
p<0.0001
n=150 n=150
Mean
Median
Ratio PM/cytosol fluorescence intesity
BM EZ
2xPH^EVCT2
C
PS sensor 2xPH^EVCT2
DMSO
NAA[10]^60min
p<0.0001
n=150 n=150
Mean
Median
Ratio PM/cytosol fluorescence intesity
DMSO NAA[10]^60min
2xPH^EVCT2
D
Lti6b
2xPH^FAPP1
P4M
2xPH^PLC
Tubbyc
1xPASS
KA1^MARK1
Elongation zone (EZ)
Basal meristem (BM)
WT
pss1-3
PI4P
PI(4,5)P2
PA
charge
E
charge
PA
PI4P
KA1^MARK1 ratio PM/cytosol fluorescence intensity
1xPASS ratio PM/cytosol fluorescence intensity
P4M ratio PM/cytosol fluorescence intensity
a n=140
b 140
c 140
c 140
a n=110
a 110
b 90
c 90
a n=150
b 150
b 140
c 140
BM EZ BM EZ
WT pss1-3
F
Total fluorescence intensity
n.s.
n=20 20
21 21
18 18
BM EZ
Lti6b
C2^LACT
2xPH^EVCT2

**Fig. S1. Localization of anionic lipid and charge sensors along the root. A.** Schematic representation of *Arabidopsis* root with the position of the respective zone of the root. Drawing by B. Peret: https://figshare.com/articles/Primary_and_lateral_root_ai/5143987. **B-C**, Confocal images of mCIT-2xPH$_{EVCT2}$ (phosphatidylserine, PS sensor) root epidermis in basal meristem (BM) and elongation elongation (EZ) in the absence/presence of NAA (10µM, 60min) and related quantification. **D-E**, Confocal images of *UBQ10prom::2xmCHERRY-Lti6b*, *UBQ10prom::mCIT-2xPH$_{FAPP1}$* (PI4P sensor), *UBQ10prom::mCIT-P4M* (PI4P sensor), *UBQ10prom::mCIT-2xPH$_{PLC}$* (PI(4,5)$P_2$ sensor), *UBQ10prom::mCIT-TUBBY-C* (PI(4,5)$P_2$ sensor), *UBQ10prom::mCIT-1xPASS* (PA sensor) and *UBQ10prom::mCIT-KA1$_{MARK1}$* (membrane surface charge sensor) in the elongation zone (EZ) and basal meristem (BM) in the wild-type and *pss1-3* background, and related quantification of plasma membrane/cytosol (PM/cytosol) ratio for mCIT-KA1$_{MARK1}$, mCIT-1xPASS and mCIT-P4M. **F**, Quantification of the total fluorescence intensity in the elongation zone (EZ) and basal meristem (BM) of *UBQ10prom::2xmCHERRY-Lti6b*, *UBQ10prom::mCIT-C2$_{LACT}$* and *UBQ10prom::mCIT-2xPH$_{EVCT2}$*. n represents the number of cells (B-C and E) and roots (F) analyzed. Scale bars 10µm, letters indicate statistical differences (see methods for details on statistical tests).

Only C2$_{LACT}$ and 2xPH$_{EVCT2}$ markers have a reduced plasma membrane/cytosol ratio in the elongation zone compared to the basal meristem (Fig. 1A and S1B). By contrast, membrane surface charges, PA and PI4P markers show the reverse tendency, with an increase plasma membrane/cytosol ratio in the elongation zone compared to the basal meristem (Fig. S1E). Note that all the analyzed constructs are driven by the same promoter (*UBQ10* promoter), and that both C2$_{LACT}$ and 2xPH$_{EVCT2}$ phosphatidylserine sensors are expressed at similar levels in the elongation zone and basal meristem (Fig. S1F). Together, these results suggest that the differential accumulation of phosphatidylserine sensors at the plasma membrane in different zone of the root is a specific property of phosphatidylserine binding proteins/domains (likely due to differential phosphatidylserine accumulation at the plasma membrane), rather than a general feature of membrane electrostatics or anionic lipids.

As expected from our previous analyses (*10*), quantitative analyses in the *pss1* mutant show a slight decrease in plasma membranes electrostatics as compared to the wild type in both basal meristem and elongation zone (as quantified with the mCIT-KA1$_{MARK1}$ membrane surface charge marker, Fig. S1D-E). Furthermore, both PA and PI4P sensors were slightly more elevated at the plasma membrane in the *pss1* mutant compared to the wild type, likely as a compensatory mechanism due to the absence of phosphatidylserine (Fig. 1E). Together, these quantifications suggest that in the absence of phosphatidylserine, there is only a slight decrease in plasma membrane electrostatics, perhaps compensated by the reciprocal increase in PA/PI4P.

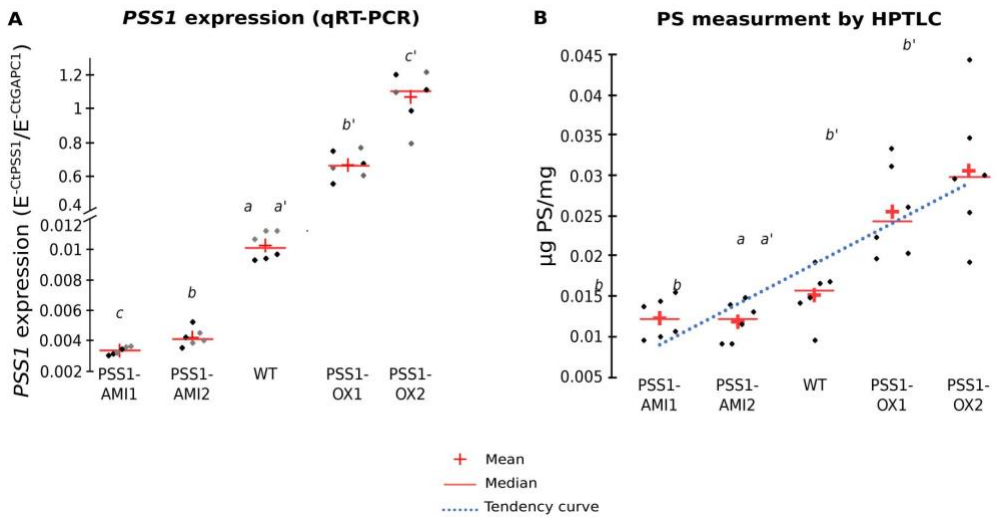


**Fig. S2. Characterization of transgenic lines with graded phosphatidylserine levels. A**, qRT-PCR analysis of *PSS1* expression in *WT*, *PSS1-AMI1*, *PSS1-AMI2*, *PSS1-OX1* and *PSS1-OX2*. *PSS1-AMI1* and *PSS1-AMI2* are two independent transgenic lines each expressing a different artificial microRNA constructs targeting *PSS1* (see the construct section of the Materials and Methods for details). *PSS1-OX1* and *PSS1-OX2* are two independent transgenic lines each overexpressing *PSS1* cDNA (same construct, *UBQ10prom::PSS1cDNA-mCITRINE*). Grey and black dots represent results obtained with different primers used to amplify the *PSS1* cDNA (see the RT-PCT section of tha Materials and Methods for details). **B**, Quantification of the phosphatidylserine content by HP-TLC in *WT*, *PSS1-AMI1*, *PSS1-AMI2*, *PSS1-OX1* and *PSS1-OX2*. Note that *pss1-3* and *pss1-4* were previously shown to produce no phosphatidylserine (*10*).

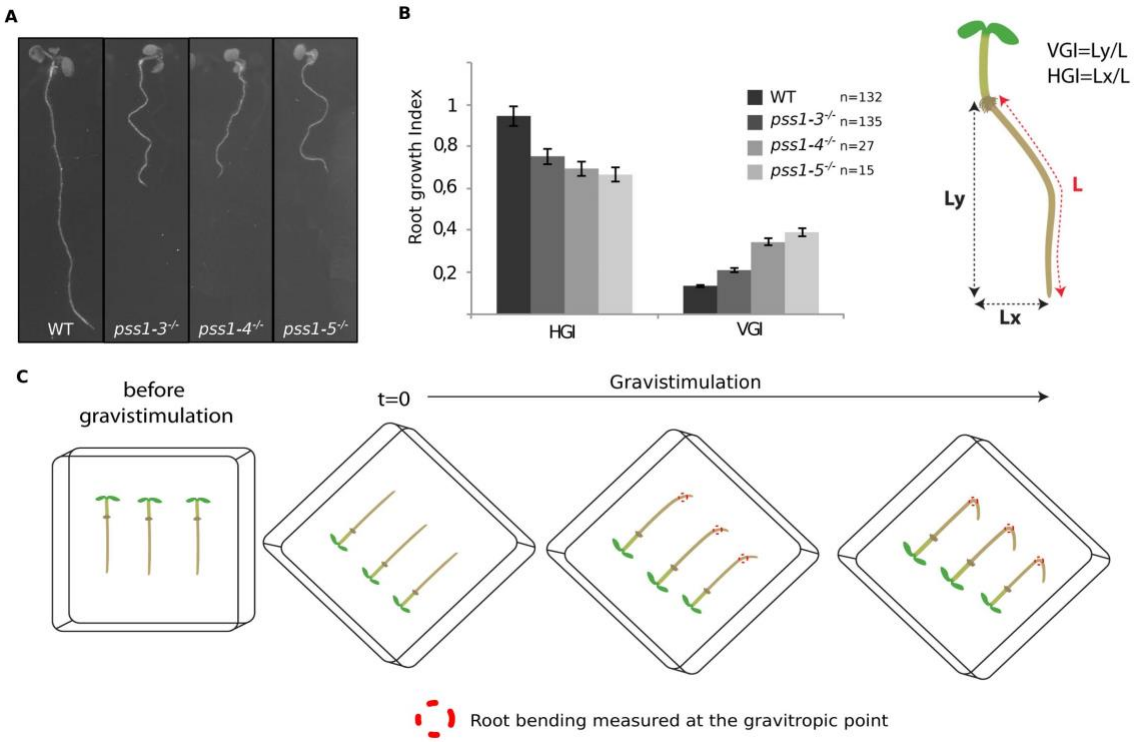


**Fig. S3. *pss1* gravitropic phenotype and method for quantification of the gravitropic response. A**, Picture showing the wavy root phenotype of *pss1-3*$^{-/-}$, *pss1-4*$^{-/-}$ and *pss1-5*$^{-/-}$, compared to the WT at 12 days after germination (DAG). **B**, Quantification of the horizontal growth index (HGI) and vertical growth index (VGI) in WT, *pss1-3*$^{-/-}$, *pss1-4*$^{-/-}$ and *pss1-5*$^{-/-}$ at 12 DAG. HGI and VGI were calculated as shown on the cartoon on the right (see (*47*) and the phenotyping section of the Materials and Methods for details). **C**, Schematic representation of the phenotypic pipeline used to analyze the gravitropic response. A time zero, plants were turned by 135° and root bending at the gravitropic point was analyzed using the RootTrace software (see the phenotyping section of the Materials and Methods for details).

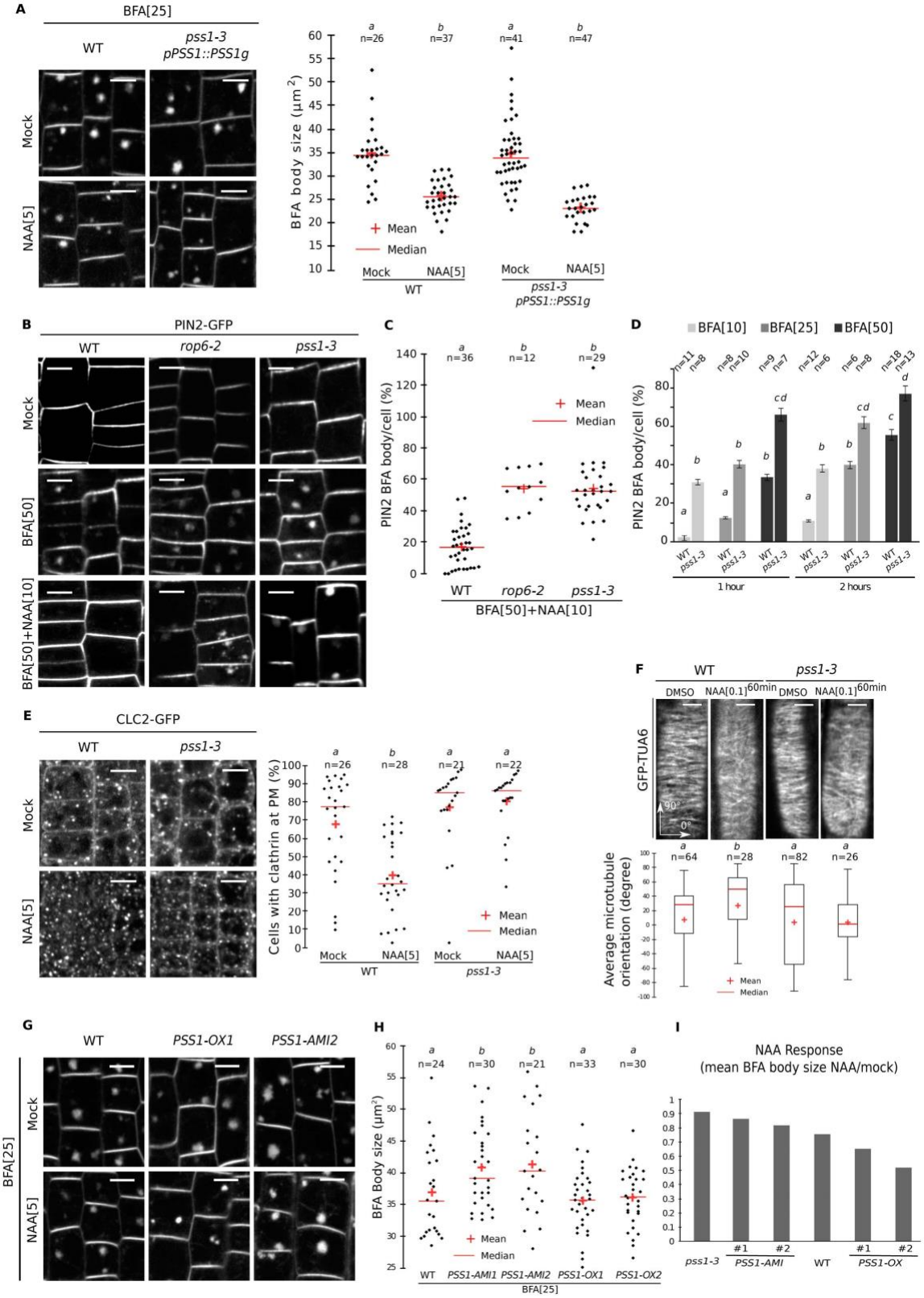


**Figure S4. Variations in phosphatidylserine impacts ROP6-mediated auxin responses. A**, Confocal images of epidermal root cells stained by FM4-64 and treated with BFA (25µM) or BFA/NAA (5µM), and related quantification of the size of FM4-64-stained BFA bodies in wild type and

complemented *pss1-3/PSS1::PSS1g* line (BFA: 25µM, 60 min; NAA: 5µM, 30min pre-treatment and 60 min co-treatment with BFA) (image and data in WT are the same as in Fig. 2C). **B**, Confocal images of 10-12-day-old seedlings expressing PIN2prom::PIN2-GFP in wild type, *rop6-2*$^{-/-}$, *pss1-3*$^{-/-}$ (upper panel) and treated with either BFA (50µM, 60 min) or BFA and NAA (10µM, 30 min pre-treatment + 60 min concomitant treatment). **C**, Quantification of the number of PIN2-GFP-positive BFA body number per cell in the wild-type, *rop6-2*$^{-/-}$ and *pss1-3*$^{-/-}$ background concomitantly treated with BFA (50µM, 60 min) and NAA (10µM, 30 min pre-treatment + 60 min concomitant treatment). **D**, Quantification of the number of PIN2-GFP-positive BFA body number per cell in wild-type and *pss1-3*$^{-/-}$ treated with increasing concentration of BFA for one or two hours. **E**, Confocal picture of root epidermal cells expressing CLC2-GFP in the wild-type and *pss1-3* background in the presence or absence of NAA (5µM, 30min) and related quantification of the percentage of cell with visible CLC2-GFP labelling at the plasma membrane (PM) (i.e. not considering CLC2-GFP in intracellular compartments). Note that in wild-type non-treated cells, CLC2-GFP localize at both the plasma membrane and intracellular compartments but that auxin selectively depletes the plasma membrane pool of CLC2-GFP. **F**, Confocal images of 12-day-old epidermal root cells expressing TUA6-GFP in wild type and *pss1-3*$^{-/-}$ in presence and absence of NAA (100nM, 60min) and related quantification of the average microtubule orientation. The average microtubule orientation was calculated using the FibriTool software (see (*48*) and the image quantification section of the Material and Methods for details). **G**, Representative images of confocal micrograph of FM4-64 staining in root epidermis treated with BFA (25µM, 60min, top) or pre-treated with NAA (5µM, 60min) and then co-treated with BFA+NAA (BFA: 25µM, 30min, NAA: 5µM, 60min). Note that the images for the wild type are the same as in Fig. 2D. **H**, quantification of the size of FM4-64-stained BFA bodies. **I**, Ratio of the mean size of FM4-64-stained BFA bodies in the NAA and mock conditions (allows us to represent the respective NAA response of each line). Scale bars 10µm. n represents the number of roots analyzed, letters indicate statistical difference (see methods for details on statistical tests).

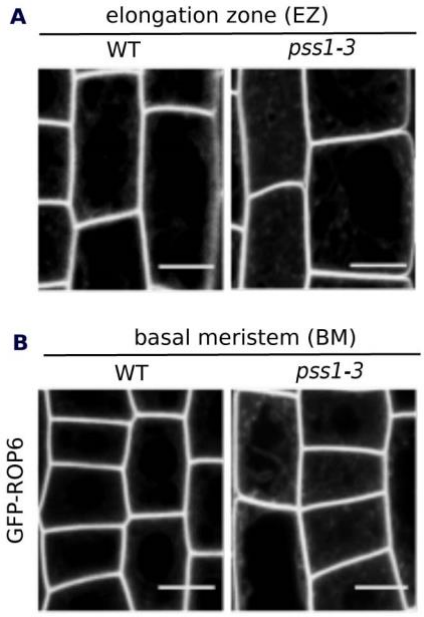


**Figure S5. Phosphatidylserine is dispensable to efficiently target ROP6 at the plasma membrane. A-B,** Confocal images of GFP-ROP6 in root epidermis in the wild type and *pss1-3* background in the elongation zone (EZ) and basal meristem (BM). Note that GFP-ROP6 is still efficiently targeted to the plasma membrane in *pss1-3*, although we noticed a faint delocalization of GFP-ROP6 in intracellular compartments. Scale bars 10µm.

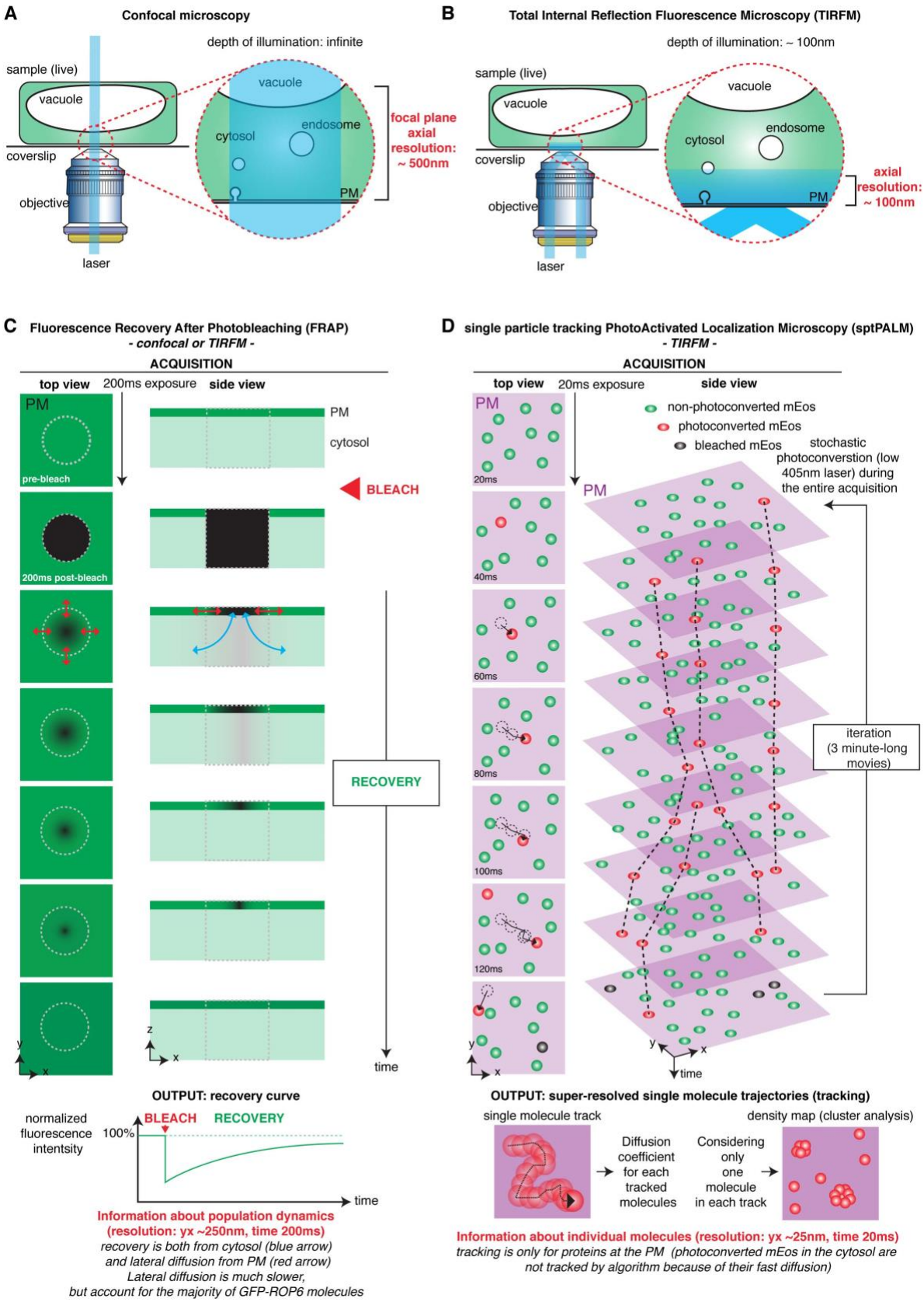
A
Confocal microscopy
depth of illumination: infinite
sample (live)
vacuole
coverslip
objective
laser
vacuole
cytosol
endosome
PM
focal plane
axial
resolution:
~ 500nm
B
Total Internal Reflection Fluorescence Microscopy (TIRFM)
depth of illumination: ~ 100nm
sample (live)
vacuole
coverslip
objective
laser
vacuole
cytosol
endosome
PM
axial
resolution:
~ 100nm
C
Fluorescence Recovery After Photobleaching (FRAP)
- confocal or TIRFM -
ACQUISITION
top view
200ms exposure
side view
PM
pre-bleach
200ms post-bleach
PM
cytosol
BLEACH
RECOVERY
time
OUTPUT: recovery curve
normalized
fluorescence
intentsity
100%
BLEACH
RECOVERY
time
Information about population dynamics
(resolution: yx ~250nm, time 200ms)
recovery is both from cytosol (blue arrow)
and lateral diffusion from PM (red arrow)
Lateral diffusion is much slower,
but account for the majority of GFP-ROP6 molecules
D
single particle tracking PhotoActivated Localization Microscopy (sptPALM)
- TIRFM -
ACQUISITION
top view
20ms exposure
side view
PM
20ms
40ms
60ms
80ms
100ms
120ms
non-photoconverted mEos
photoconverted mEos
bleached mEos
stochastic
photoconverstion (low
405nm laser) during
the entire acquisition
PM
iteration
(3 minute-long
movies)
time
OUTPUT: super-resolved single molecule trajectories (tracking)
single molecule track
density map (cluster analysis)
Diffusion
coefficient
for each
tracked
molecules
Considering
only
one
molecule
in each track
Information about individual molecules (resolution: yx ~25nm, time 20ms)
tracking is only for proteins at the PM (photoconverted mEos in the cytosol are
not tracked by algorithm because of their fast diffusion)

**Fig. S6: Principle underlying the TIRFM, FRAP and sptPALM analyses**. **A**, In confocal microscopy (both laser scanning and spinning-disk confocal microscopy), the illumination beam of the laser is perpendicular to the coverslip and passes through the entire sample, exciting all the fluorophores. The focal plane is determined by the pinhole(s) of the confocal microscope and provides an axial resolution (z position) of about 500nm. **B**, In Total Internal Reflection Fluorescence Microscopy (TIRFM), the illumination beam is oriented at a critical angle when it hits the interface between the coverslip and the sample. In this condition, the beam is reflected, which locally generates an evanescent wave of low energy that penetrates the sample up to about 100nm. As such, only fluorophores that are in close contact with the coverslip are excited, which provides an axial resolution of about the depth of the evanescent wave (~100nm). TIRFM is therefore particularly well suited to study events happening at or in the close vicinity of the plasma membrane (PM) in contact with the coverslip. Because fluorophores outside of the evanescent wave are not excited, this technique dramatically increases the signal-to-noise ratio during imaging, which allows faster acquisition (and/or single molecule imaging). While the xy resolution is still limited (~250nm), the fact that TIRFM largely deplete out-of-focus fluorescence allows to visualize structures, which are in the plane of the plasma membrane, and that are not easily identifiable by confocal microscopy. Schematic representation was inspired by Johnson and Vert, 2017 (*51*). **C**, Fluorescence Recovery After Photobleaching (FRAP) is a technique to study the kinetics of diffusion of fluorescent molecules. It is based on the fact that a focused high intensity illumination will selectively photobleach the fluorophore (i.e. permanently unable to fluoresce) on a determined region of the sample (here, a small portion of the plasma membrane). Through time, the still-fluorescing GFP-ROP6 molecules will diffuse and replace the dark molecules in the bleached region. FRAP provides information about the diffusion dynamics of the population of GFP-ROP6 molecules (i.e. it provides an averaged value of diffusion, but cannot distinguished whether some proteins are diffusing slowly and some others rapidly, or whether their diffusion is uniform). In addition, fluorescence may be recovered from GFP-ROP6 diffusing in the membrane or arriving from the cytosol. Finally, FRAP can be recorded either in confocal microscopy (see Fig. 3A, 4A and S7) or TIRFM acquisition (see Fig. 4E). **D**, Single particle tracking PhotoActivated Localization Microscopy (sptPALM) is a super-resolution microscopy method, which is a derivative of the PALM technique. PALM uses the stochastic activation of photoactivable (or photoswitchable in the case of mEos) fluorescent proteins to perform single molecule imaging. Photoactivation is performed with low light intensity, so that only a small fraction of the molecules is activated, and therefore photoactivated proteins are well separated from each other during imaging. In order to image single molecules, a microscopy setup with a high signal-to-noise ratio, such as TIRFM, is required. In the framework of our study on ROP6 and phosphatidylserine, TIRFM is an ideal technique since it allowed us to preferentially focus on the pool of ROP6/phosphatidylserine at the plasma membrane. Each single molecule is recorded as a diffraction limited spot that can be fitted and thereby positioned with high accuracy (xy resolution of about 25nm). PALM is usually performed on fixed samples and the photoactivated proteins are immediately photobleached during the acquisition (excitation with high laser intensity), so that the position of each molecule is recorded only once. The super-resolved image is built through successive cycle of photoactivation followed by acquisition of the single molecules position and its concomitant photobleaching. The main difference between PALM and sptPALM is that sptPALM is performed on live samples (i.e. with molecules diffusing during the time lapse acquisition) and photoactivated molecules are not immediately photobleached during acquisition (excitation with mild laser intensity). This allows to track the positions of single molecules through

time before the photoactivated fluorescent protein is bleached (or detached from the plasma membrane). This technique thereby allows to obtain the trajectories of single molecules with a xy resolution of roughly 25nm and time resolution of 20ms. It is then possible to obtain a range of quantitative parameters from these tracks, including a spatial map of the trajectories (as shown on Fig. 3D), or their diffusion coefficient (as shown on Fig. 3D, 4D, 5B and F, S9, S11, S12 and S16). By considering only the position of one molecule per track, we can build "livePALM" images, which shows the average position of each mEos-ROP6 molecule imaged during the acquisition (3-minute-long movies). This provides a density map of mEos-ROP6 and allows us to perform cluster analyses (in our case using Voronoï tessellation, see Fig. 3E-F, 5A and S10). By contrast to FRAP, which provides a global analysis of diffusion at the scale of the bleached fluorescent protein population, sptPALM gives access to single molecules information. Furthermore, sptPALM/TIRFM has also increased resolution in all dimensions (z ~100nm, xy ~25nm, t=20ms vs z ~500nm, xy ~250nm, t=200ms in FRAP/confocal).

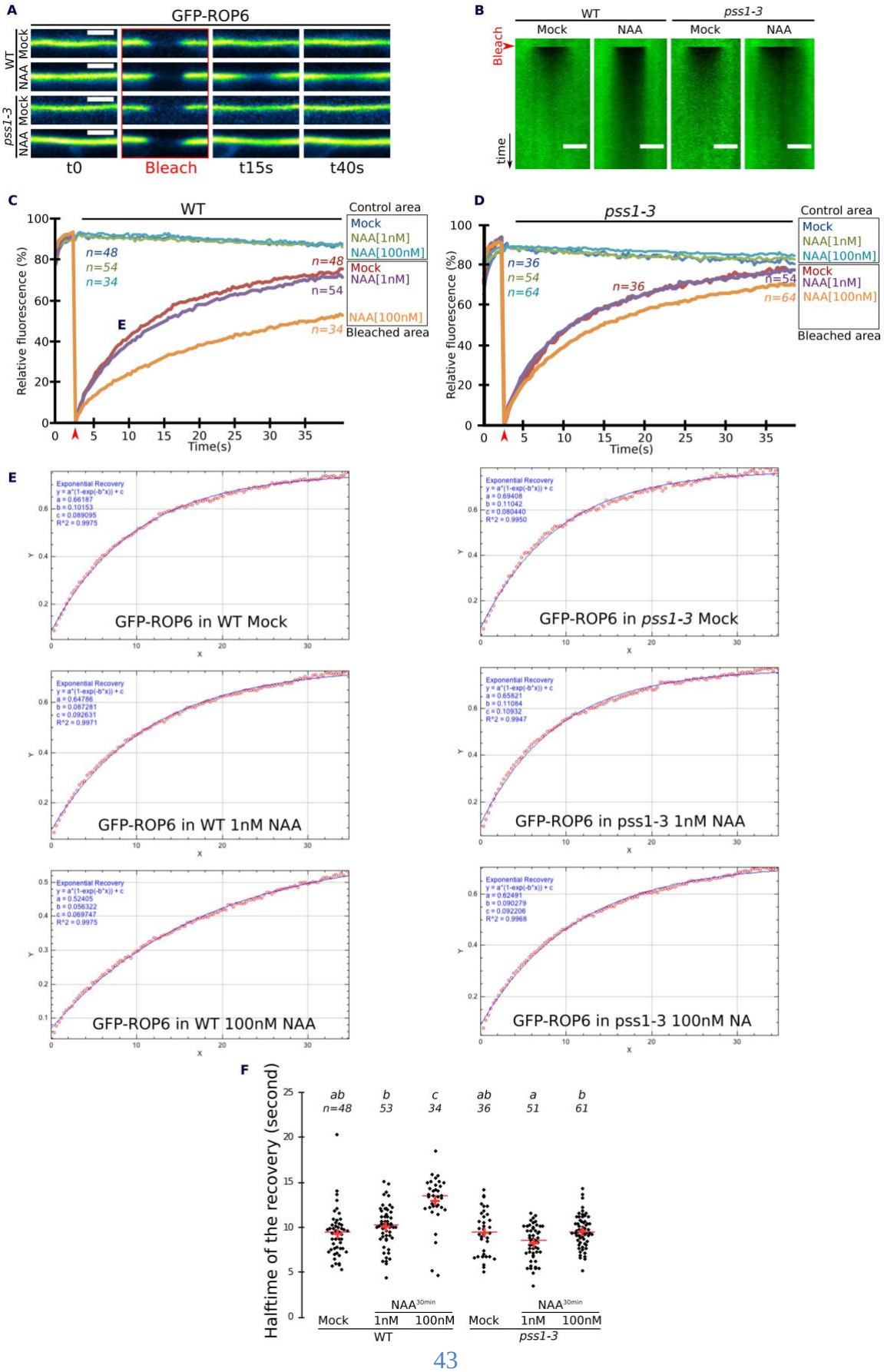
A
GFP-ROP6
WT
Mock
NAA
pss1-3
Mock
NAA
t0
Bleach
t15s
t40s
B
WT
pss1-3
Mock
NAA
Mock
NAA
Bleach
time
C
WT
Control area
Mock
NAA[1nM]
NAA[100nM]
Bleached area
n=48
n=54
n=34
n=48
n=54
n=34
E
Relative fluorescence (%)
Time(s)
D
pss1-3
Control area
Mock
NAA[1nM]
NAA[100nM]
Bleached area
n=36
n=54
n=64
n=36
n=54
n=64
Relative fluorescence (%)
Time(s)
E
Exponential Recovery
y = a*(1-exp(-b*x)) + c
a = 0.66187
b = 0.10153
c = 0.089095
R^2 = 0.9975
GFP-ROP6 in WT Mock
Exponential Recovery
y = a*(1-exp(-b*x)) + c
a = 0.69408
b = 0.11042
c = 0.080440
R^2 = 0.9950
GFP-ROP6 in pss1-3 Mock
Exponential Recovery
y = a*(1-exp(-b*x)) + c
a = 0.64786
b = 0.087281
c = 0.092631
R^2 = 0.9971
GFP-ROP6 in WT 1nM NAA
Exponential Recovery
y = a*(1-exp(-b*x)) + c
a = 0.65821
b = 0.11084
c = 0.10932
R^2 = 0.9947
GFP-ROP6 in pss1-3 1nM NAA
Exponential Recovery
y = a*(1-exp(-b*x)) + c
a = 0.52405
b = 0.056322
c = 0.069747
R^2 = 0.9975
GFP-ROP6 in WT 100nM NAA
Exponential Recovery
y = a*(1-exp(-b*x)) + c
a = 0.62491
b = 0.090279
c = 0.092206
R^2 = 0.9968
GFP-ROP6 in pss1-3 100nM NA
F
Halftime of the recovery (second)
ab
n=48
b
53
c
34
ab
36
a
51
b
61
NAA30min
Mock
1nM
100nM
WT
Mock
1nM
100nM
pss1-3

**Figure S7. Fluorescence recovery analyzes of GFP-ROP6 in the absence and presence of exogenous auxin treatment. A**, Confocal images of GFP-ROP6 during FRAP experiment in wild type (WT) and *pss1-3* in the mock and auxin-treated condition (NAA, 100nM, 30 min), and **B**, related kymograph (time scale 9 seconds). **C-D**, Traces of GFP-ROP6 fluorescence intensity at the plasma membrane during FRAP analyses in mock and NAA (30min at 1nm or 100nm) treated conditions in WT and *pss1-3* roots. **E**, Fitted GFP-ROP6 fluorescence recovery curve used to determine the halftime of the fluorescence recovery in mock and NAA (30 min at 1 nm or 100 nm) treated conditions in wild-type and *pss1-3* roots. **F**, Quantification of the halftime of the fluorescence recovery in mock and NAA (30 min at 1 nm or 100 nm) treated conditions in wild-type and *pss1-3* roots. Kymograph images for the wild type are the same as in Fig. 3A. Scale bars: 5 µm. n represents the number of ROI analyzed, letters indicate statistical difference (see methods for details on statistical tests).

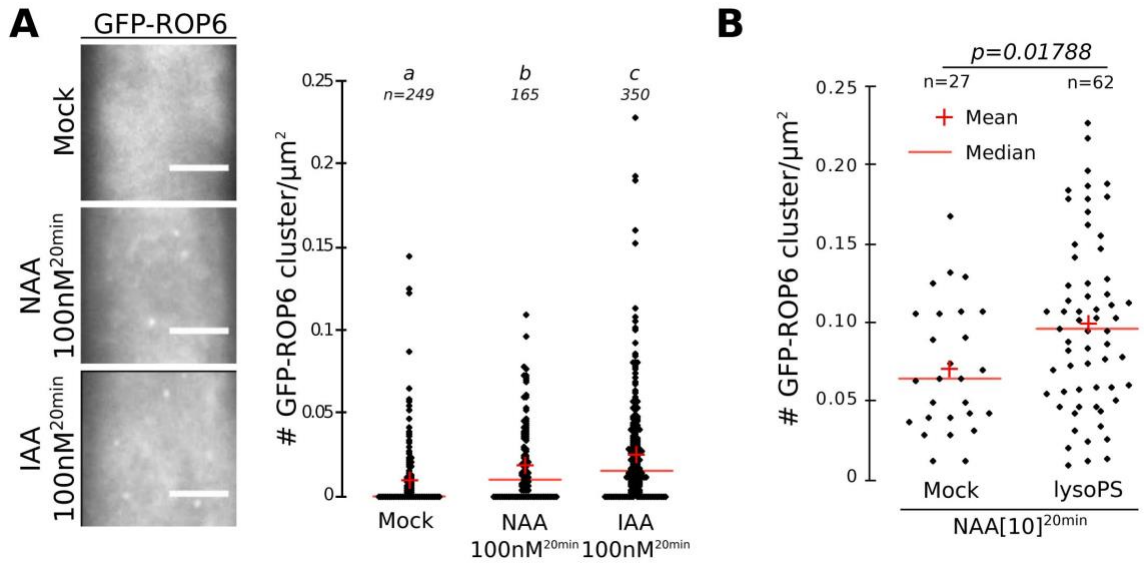


**Fig. S8. TIRFM analyses of GFP-ROP6 clustering in response to NAA, IAA and lysophosphatidylserine. A**. TIRFM micrograph of GFP-ROP6 in the basal meristem in response to NAA (100 nM, 20 min) or IAA (100 nM, 20 min) and related quantification (quantifications were performed as in Fig. 3B and include cells from both basal meristem and elongation zone). **B**. Quantification of TIRFM experiment in the presence or absence of lysophosphatidylserine (lysoPS) in the meristematic region (NAA: 10 µM, 20min) (quantifications were performed as in Fig. 3B and include cells from both basal meristem and elongation zone). Based on yeast and animal literature, lysophosphatidylserine is quickly (~10 min) converted to double chain phospholipids (*i.e.* phosphatidylserine). This is happening in the Endoplasmic Reticulum (ER) membrane and phosphatidylserine is then transferred to the plasma membrane (PM) at ER/PM contact sites by the action of OSBP-Related Domain (ORD)/Osh proteins (*52-54*). Furthermore, in animal cells, exogenous phosphatidylserine treatment leads to the quick remodeling of their acyl chain, in a PLA2-dependent manner (*55*). While it is currently unknown whether similar remodeling is happening in plants, it is likely the case. It is therefore possible that the fatty acyl chains of phosphatidylserine may be important for the regulation of ROP6 (*i.e.* the effect may not be directly mediated by lysophosphatidylserine, but by phosphatidylserine itself, perhaps with a certain type of acyl chains). Whether phosphatidylserines of specific fatty acyl composition are involved in ROP6 nanoclustering remains on open question, which will need to be investigated further in the future.

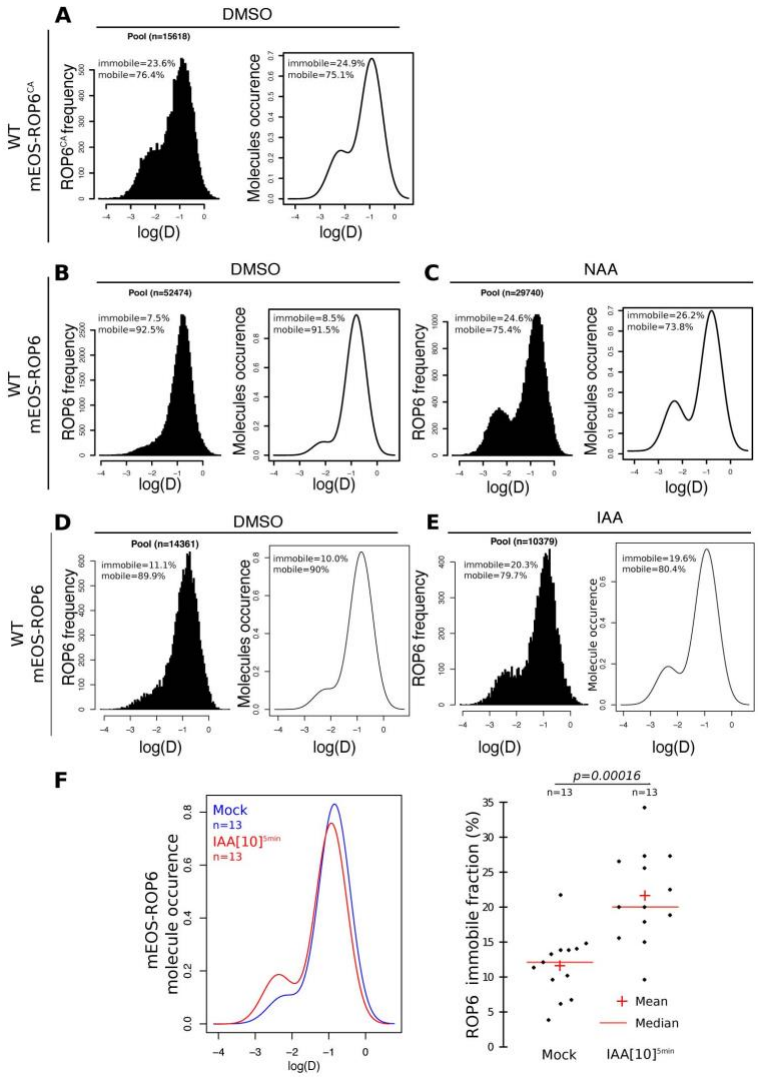


**Fig. S9. Raw data of sptPALM experiments presented in Figure 3 and analysis of mEOS-ROP6 response to IAA. A-E**, Left panel represents the frequency of mEos-ROP6CA and mEos-ROP6 molecules according to their apparent diffusion coefficient (log(D)) obtained by analyzing sptPALM trajectories in mock and auxin-treated condition (NAA, 10µM, 5min; IAA, 10µM, 5min) in the wild-type background. Right panel represents the distribution of mEos-ROP6CA and mEos-ROP6 molecules according to their apparent diffusion coefficient (log(D)) obtained by analyzing the frequency plot (left panel) using the R mClust package. The percentage of immobile and mobile molecules in each graph represents the percentage of molecules with a trajectory below and above the log(D) of -1.75, respectively. Note that the percentage in left and right panels for each condition are similar (i.e. they vary only from few percent), confirming the existence of two populations with a normal distribution. Note that the right plots in B and C were combined to produce the plot in Fig. 3D, and the right plots in D and E were combined to produce the left plot in Fig. S9F. "n" corresponds to the number of trajectories analyzed. **F**, Quantification of mEos-ROP6 immobile fraction in the absence or presence of IAA (10µM, 5min). "n" corresponds to the number of independent acquisitions (independent cells).

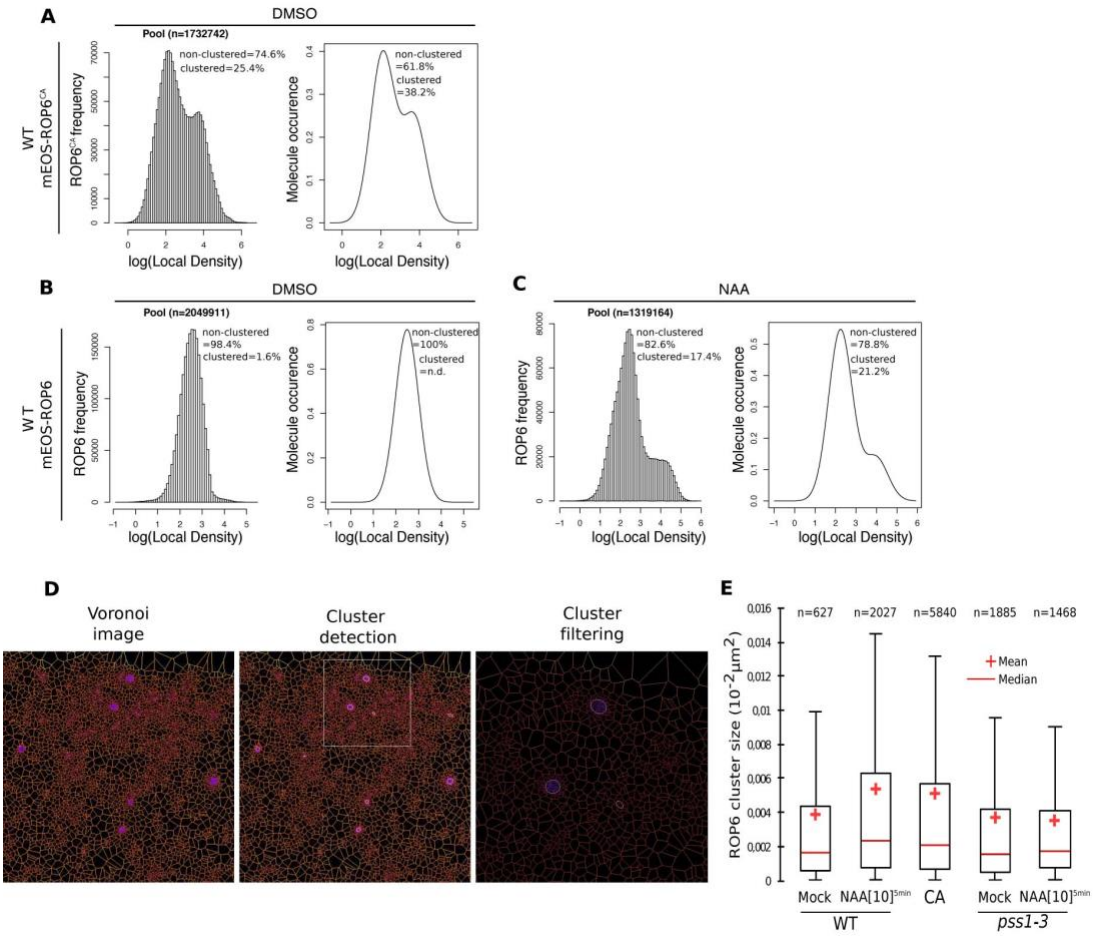


**Fig. S10. Raw data of live PALM experiments presented in the paper.** **A-C**, Left panels represents the frequency of mEos-ROP6 and mEos-ROP6CA molecules according to their local density (log(local density)) obtained by analyzing tessellation-based automatic segmentation of super-resolution images in mock and auxin-treated condition (NAA, 10µM, 5min) in the wild type. Right panel represents the distribution of mEos-ROP6 and mEos-ROP6CA according to their local density (log(local density)) obtained by analyzing the frequency plot (left panel) using the R mClust package. The percentage of low and high local density in each graph represents the percentage of molecules below and above the log(local density) of 3.5, respectively. Note that the percentage in left and right panels for each condition are similar (i.e. they vary only from few percent), confirming the existence of two populations with a normal distribution. Note that the right plots in B and C were superposed to produce the plots in Fig. 3F. "n" corresponds to the number of molecules analyzed. **D**, Example of Voronoï images obtained after extracting local density from tessellation-based automatic segmentation of super-resolution images (left image), cluster detection and filtering of local density (middle image, zoom in right image) in the Voronoï image and **E**, quantification of the respective size of the cluster in (from left to right), mEos-ROP6 mock-treated, mEos-ROP6 NAA-treated (5min, 10µM), mEosROP6CA mock-treated, mEos-ROP6 mock-treated in *pss1-3* and mEos-ROP6 NAA-treated in *pss1-3* (5min, 10µM). "n" corresponds to the number of nanoclusters analyzed.

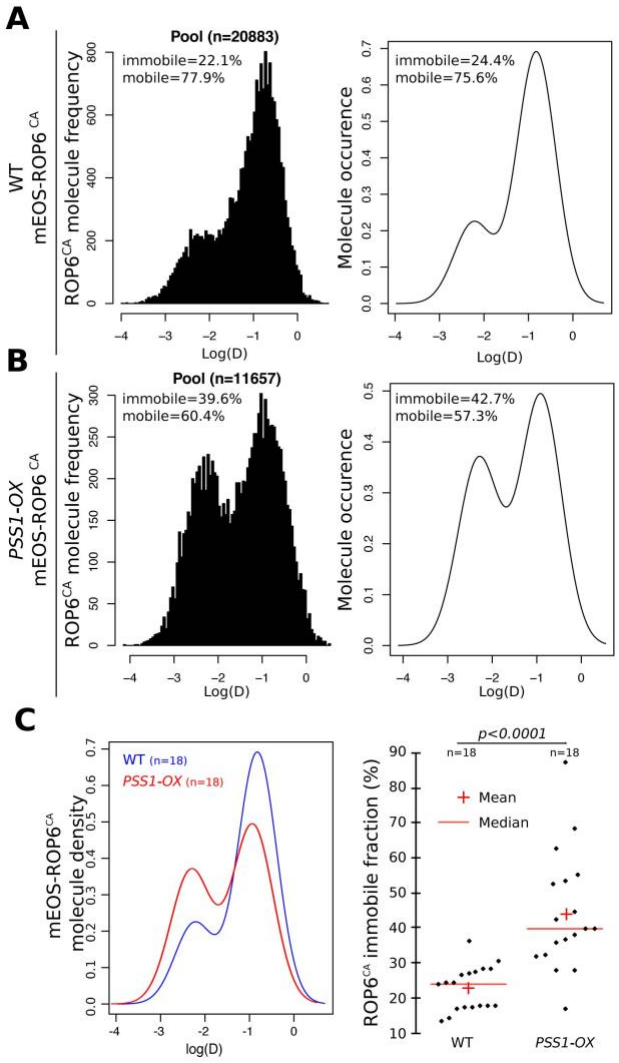


**Fig. S11. sptPALM analysis of mEos-ROP6CA in the wild type and *PSS1-OX* lines. A-B**, Left panel represents the frequency of mEos-ROP6CA molecules according to their apparent diffusion coefficient (log(D)) obtained by analyzing sptPALM trajectories in the wild-type and *PSS1-OX* background. Right panel represents the distribution of mEos-ROP6CA molecules according to their apparent diffusion coefficient (log(D)) obtained by analyzing the frequency plot (left panel) using the R mClust package. The percentage of immobile and mobile molecules in each graph represents the percentage of molecules with a trajectory below and above the log(D) of -1.75, respectively. Note that the percentage in left and right panels for each condition are similar (i.e. they vary only from few percent), confirming the existence of two populations with a normal distribution. Note that the right plots in A and B were combined to produce the plot in Fig. 4D and left plot of Fig. S11C. **C**, Quantification of mEos-ROP6CA immobile fraction in the wild-type and *PSS1-OX* background. "n" corresponds to the number of independent acquisitions (independent cells).

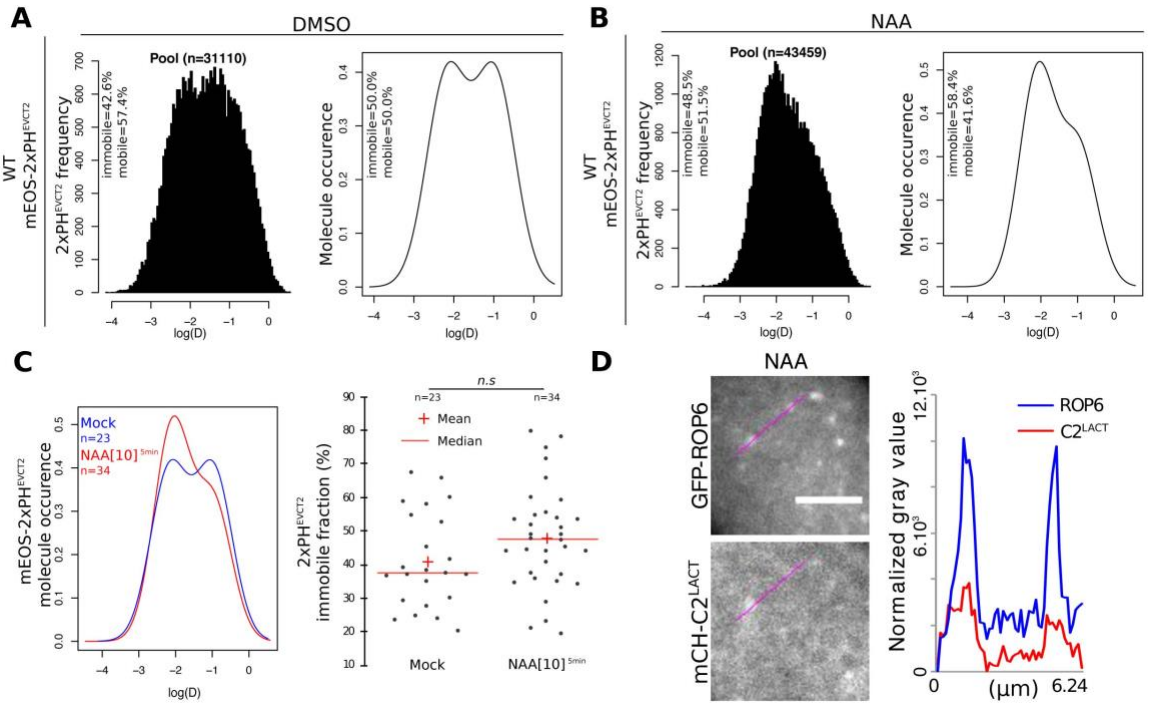


**Fig. S12. sptPALM analysis of mEos-PHEVCT2 in the absence and presence of exogenous auxin. A-B**, Left panel represents the frequency of mEos-2xPHEVCT2 molecules according to their apparent diffusion coefficient (log(D)) obtained by analyzing sptPALM trajectories in the mock and auxin-treated condition (NAA 10µM, 5min). Right panel represents the distribution of mEos-2xPHEVCT2 molecules according to their apparent diffusion coefficient (log(D)) obtained by analyzing the frequency plot (left panel) using the R mClust package. The percentage of immobile and mobile molecules in each graph represents the percentage of molecules with a trajectory below and above the log(D) of -1.75, respectively. Note that the percentage in left and right panels for each condition are similar (i.e. they vary only from few percent), confirming the existence of two populations with a normal distribution. Note that the right plots in A and B were combined to produce the plot in Fig. 5A and the left plot in Fig. S12C. **C**, Quantification of mEos-2xPHEVCT2 immobile fraction in the mock and auxin-treated condition (10µM, 5min). "n" corresponds to the number of independent acquisitions (independent cells). **D**, TIRFM micrograph of root cells co-expressing GFP-ROP6 with the phosphatidylserine marker 2xmCH-C2LACT (NAA: 10µM, 20 min) and line scan of fluorescence intensities. Scale bars 5µm.

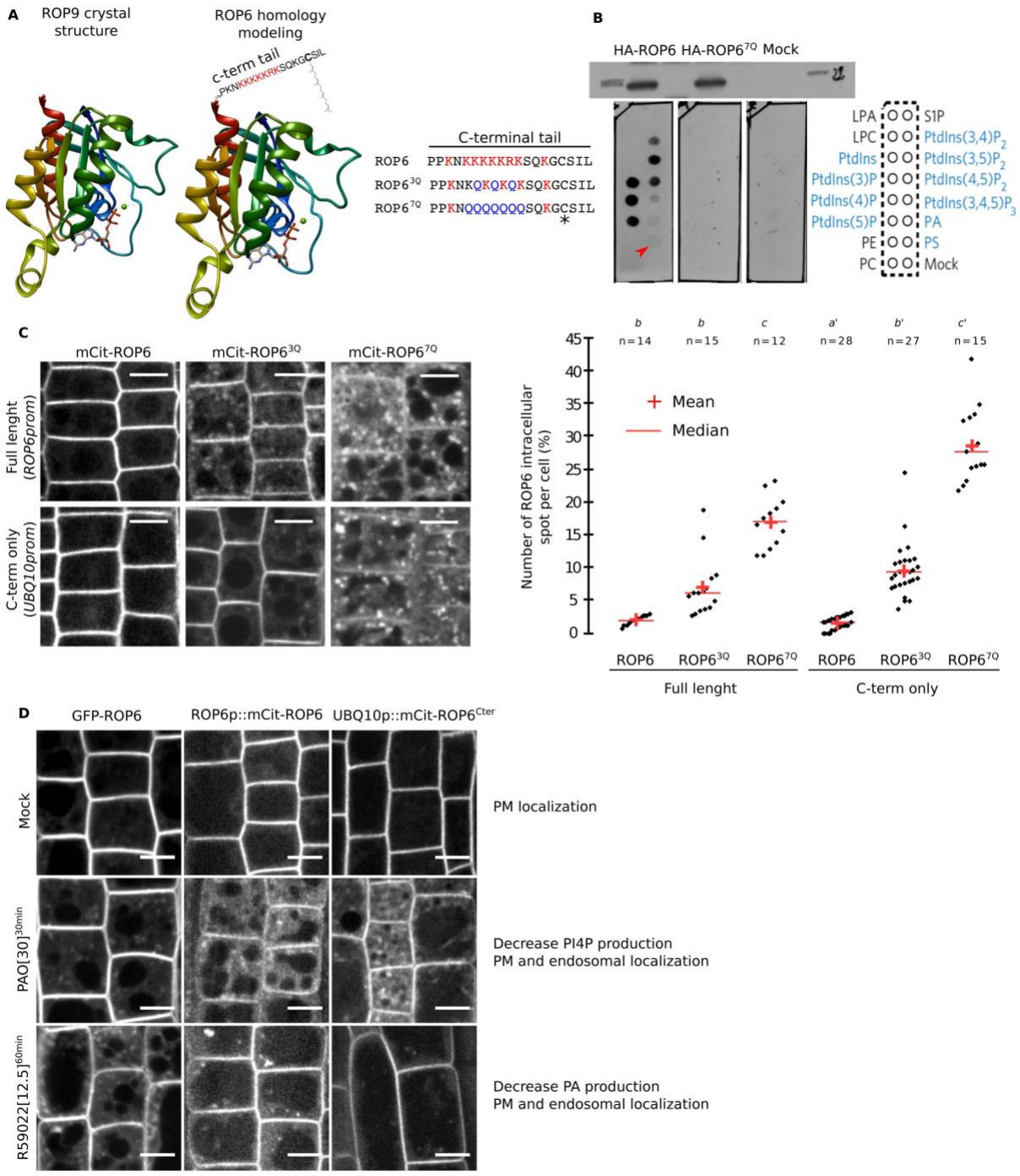


**Fig. S13. ROP6 polybasic region interacts with anionic phospholipids and is involved in plasma membrane targeting. A**, Structure of ROP9 (PDB: 2J0V) and homology model of ROP6 based on ROP9 structure. The position of ROP6 C-terminal tail (polybasic region + geranylgeranyl) is indicated as well as the sequence of ROP6, ROP6$_{3Q}$, ROP6$_{7Q}$ C-terminal tail. The asterisk indicates the cysteine required for geranylgeranylation. **B**, Western blot (top) showing expression of recombinant HA-ROP6 and HA-ROP6$_{7Q}$ and mock (empty vector) and their corresponding lipid overlay assays (bottom left). Bottom right, scheme showing the position of the different lipid species spotted on the membrane. Anionic lipids are highlighted in blue. The red

arrowhead indicates the interaction between HA-ROP6 but not HA-ROP6$_{7Q}$ with phosphatidylserine (PS). **C**, Confocal images of mCIT-tagged *ROP6*, *ROP6$_{3Q}$*, *ROP6$_{7Q}$*, *ROP6$_{Cter}$*, *ROP6$_{3Q\text{-}Cter}$*, *ROP6$_{7Q\text{-}Cter}$* and related quantification of the number of intracellular compartments per cell. n represents the number of roots analyzed, letters indicate statistical differences (see methods for details on statistical tests). **D**, Confocal images of *35Sprom::GFP-ROP6*, *ROP6prom::mCIT-ROP6* and *UBQ10-mCIT-ROP6$_{Cter}$* in the mock, PAO (30µM, 30min, PI4-Kinase inhibitor) and R599022 (12.5µM, 60min, DAG-Kinase inhibitor) treated condition.

Consistent with ROP6 polybasic region being able to interact with anionic phospholipids with an electrostatic component, ROP6 interacted with all anionic phospholipids. In addition, in this *in vitro* assay, ROP6 binding to phosphatidylserine and phosphatidic acid (PA) was weaker than binding to phosphatidylinositol phosphate (PIPs). This is expected as both PA and phosphatidylserine are less electronegative than PIPs. Nonetheless, this may not reflect the relative importance of these interactions *in vivo*, since they have different relative concentrations. We noticed that the C-terminal tail of ROP6 closely resemble the C-terminal tail of K-Ras that we recently used as a membrane surface charge sensor in plants (*10*, *20*). ROP6, like membrane surface charge sensors, possess in its C-terminus a polybasic region (PBR) adjacent to a prenylation site (i.e. geranylgeranylation for ROP6, farnesylation for K-Ras). Substitution of seven lysine residues into neutral glutamine in ROP6-PBR (ROP6$_{7Q}$) abolished *in vitro* interaction with all anionic lipids, showing that interaction with anionic phospholipids was fully dependent on the positive charges in ROP6 C-terminal tail. In planta, diminishing the net positive charges of ROP6-Cter gradually increased its mislocalization into intracellular compartments. This effect was charge dependent as mutating 3 lysine residues in the polybasic region (ROP6$_{3Q}$) had an intermediate effect on ROP6 plasma membrane targeting. Again, the graded delocalization of mutant ROP6 into intracellular compartments depending on their charges closely resembled the behavior of membrane surface charge reporters (*10*, *20*). This suggested that ROP6 plasma membrane targeting was dependent on the electrostatic potential of this membrane. Furthermore, we obtained similar results when we expressed only the C-terminal tail of ROP6 (PBR + geranylgeranylation site). Therefore, ROP6 C-terminal tail is necessary and sufficient for ROP6 plasma membrane targeting. As shown in Figure S5, phosphatidylserine has only a minor role in ROP6 plasma membrane targeting, with most of GFP-ROP6 remaining at the plasma membrane in the *pss1* mutant and only a small proportion being delocalized in intracellular compartments. This was in stark contrast with the extensive delocalization of mCIT-ROP6$_{7Q}$ in intracellular compartments. As ROP6$_{7Q}$ impaired interaction with all anionic lipids, these results suggested that interaction with additional anionic lipids are required for efficient plasma membrane targeting of ROP6. We previously demonstrated that three anionic lipids are involved in the plant plasma membrane high electrostatic signature, with PI4P playing a major role, followed by PA and then phosphatidylserine (*10*, *20*). To test whether PI4P and/or PA could be involved in ROP6 plasma membrane targeting, we inhibited their synthesis using inhibitors of PI4Kinases (i.e. PAO) and DAG Kinases (i.e. R59022). Again, we found that ROP6 localization (either full length or C-terminal tail only) behaved like membrane surface charge reporters, with inhibition of PI4P synthesis having the strongest effect on ROP6 plasma membrane targeting followed by inhibition of PA synthesis. Together, these results suggest that ROP6 is targeted to the plasma membrane, at least to some extent, via direct electrostatic interactions between the polybasic region present in ROP6 C-terminal tail and the inner electrostatic potential of the plasma membrane. Together, these results also confirm that ROP6/ phosphatidylserine interaction main functions are not plasma

membrane targeting but rather suggest a specific role for this interaction in regulating ROP6 lateral segregation within the plasma membrane. Together; these results suggest that ROP6 targeting to plasma membrane nanodomains is not purely electrostatics. Similar conclusions were recently proposed for K-Ras (which has a very similar polybasic tail as ROP6). Indeed, molecular dynamics analyzes suggest that K-Ras polybasic tail preferentially interacts with phosphatidylserine for nanocluster formation (*6*). Nonetheless, similar to ROP6, the polybasic tail of K-Ras was also demonstrated to localize to the plasma membrane via electrostatic interactions (*4*, *56*, *57*).

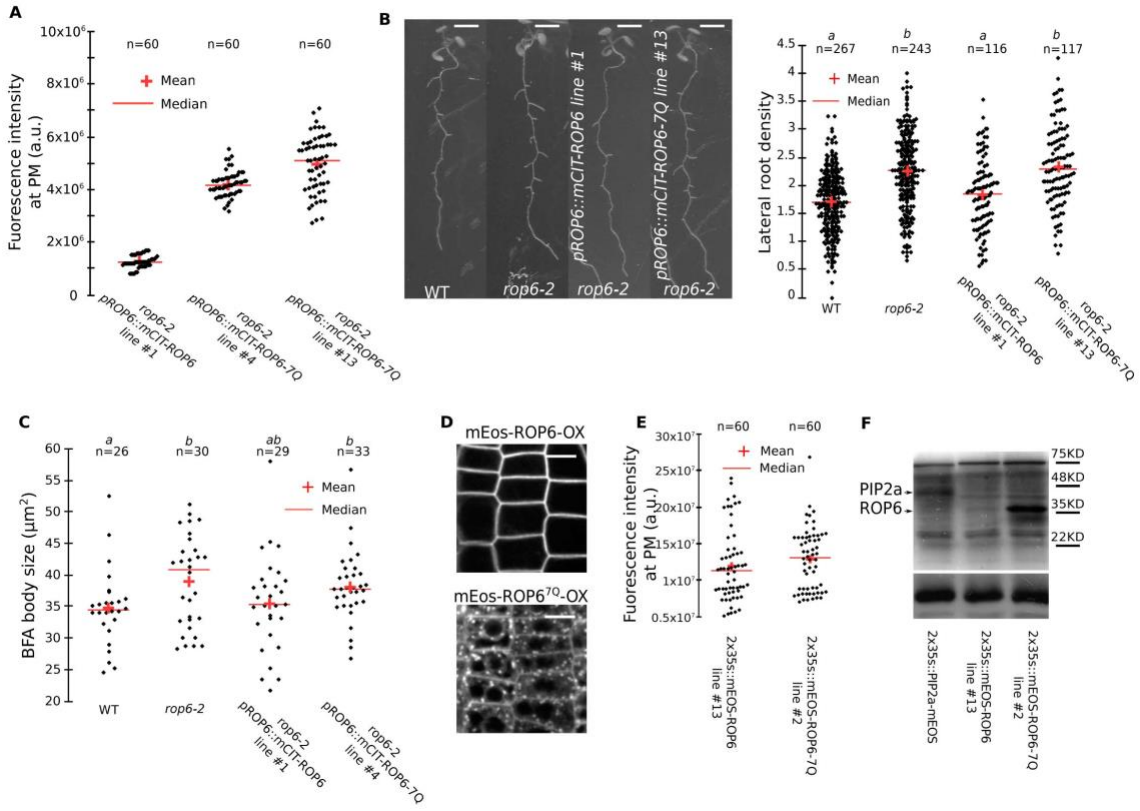


**Fig. S14. The ROP6 polybasic region is required to complement *rop6-2* loss-of-function allele and to induce *ROP6-OX* gain-of-function phenotype.** Because ROP6$_{7Q}$ is delocalized in intracellular compartments (a property that is largely regulated by PI4P and PA, rather than phosphatidylserine, see Fig. S13), we selected transgenic lines with high expression level so that they had similar (or even higher) accumulation at the plasma membrane (PM). As expected, we had to select transgenic lines that expressed overall higher amount of proteins than mEos-ROP6 (as seen using anti-mEos western blot analyzes) to have similar amount or mEos-ROP6$_{7Q}$ at the plasma membrane. This strategy allowed us to perform complementation analyses and to analyze whether plasma membrane-localized ROP6$_{7Q}$ is functional or not. **A**, Quantification of the mCITRINE signal at the plasma membrane in 7 day-old root meristem expressing *ROP6prom::mCITRINE-ROP6* and *ROP6prom::mCITRINE-ROP6$_{7Q}$* in *rop6-2$^{-/-}$* background (n=60 plasma membrane). **B**, Images of 12 day-old seedlings expressing *ROP6prom::mCITRINE-ROP6* and *ROP6prom::mCITRINE-ROP6$_{7Q}$* in *rop6-2$^{-/-}$* background showing lateral root formation, and related quantification of the lateral root density. Lateral root formation was used as a sensitive phenotypic read-out for the complementation of *rop6-2* (*16*). **C**, Quantification of BFA body size in *ROP6prom::mCITRINE-ROP6* and *ROP6prom::mCITRINE-ROP6$_{7Q}$* in *rop6-2$^{-/-}$* background. **D**, Confocal images of 7 day-old root cells overexpressing *2x35S::mEos-ROP6 and 2x35S::mEos-ROP6$_{7Q}$.* **E**, Quantification of the mEos signal at the plasma membrane (PM) in 7 day-old root meristem overexpressing *2x35S::mEos-ROP6* and *2x35S::mEos-ROP6$_{7Q}$*. **F**, Western blot showing mEos-tagged protein accumulation in the following transgenic lines (from left to right): *PIP2a::PIP2a-mEos*, *2x35S::mEos-ROP6* (line 13) and *2x35S::mEos-ROP6$_{7Q}$* (line 2). In the top panel, the blot was probed with an anti-mEos antibody and in the bottom panel with anti-Histone H3 antibody as loading control. n represents the number of roots analyzed, letters indicate statistical differences (see methods for details on statistical tests).

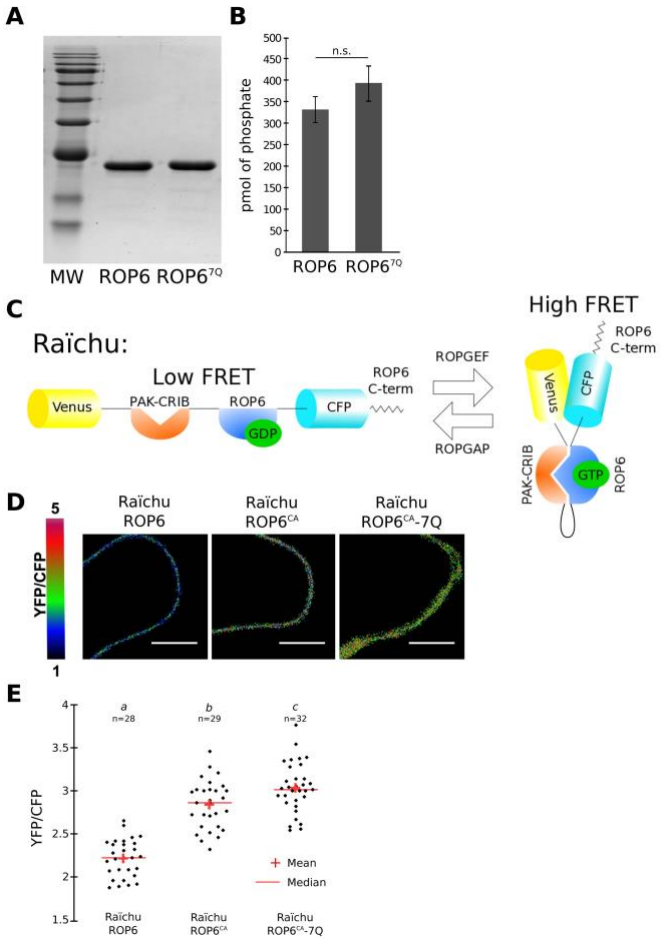


**Fig. S15. ROP6 polybasic region is not required for its GTPase activity or for interaction with effectors. A**, SDS-PAGE of purified recombinant 6His-ROP6 (full length) and 6His-ROP6$_{7Q}$. **B**, Measurement of ROP6 and ROP6$_{7Q}$ intrinsic GTPase activity. **C**, Schematic representation of the construct architecture and principle of the FRET-based sensor of ROP6 activation (RaichuROP6). **D**, Ratiometric images of Raichu-ROP6, Raichu-ROP6$_{CA}$, and Raichu-ROP6$_{CA\text{-}7Q}$ transiently expressed in *Nicotiana tabacum* (color scale shown on the left) and **e**, related quantification. n represents the number of cell analyzed, letters indicate statistical differences (see methods for details on statistical tests).

After having established that plasma membrane-localized ROP6$_{7Q}$ are not functional, we verified that mutating the polybasic region did not impacted ROP6 GTPase activity and/or its ability to bind downstream effectors when in a GTP-bound conformation. For this purpose, we purified full length ROP6 (including the entire C-terminal tail with or without the 7Q mutation) and tested its intrinsic GTPase activity (i.e. ability to hydrolyze GTP in solution). This assay showed that the 7Q mutation in ROP6 C-terminal tail did not impacted the enzymatic activity of the GTPase domain. We also developed a ratiometric FRET-based sensor of ROP6 activity based on the design of the Rho GTPase biosensors for Rac/Cdc42 named Raichu-Rac1 and Raichu-Cdc42 (*35*, *37*). In Raichu-Rac1/Cdc42 sensors, the CRIB domain of human PAK1 is cloned in tandem with Rac1 or Cdc42 (interspaced by an appropriate linker) and flanked by two fluorescent protein FRET pairs (Venus and ECFP). The CRIB domain interacts specifically with activated Rac1/Cdc42 (i.e. GTP-bound Rac1 or Cdc42), which induces a conformational change in the sensor and enhances the FRET efficiency between the two fluorescent proteins. We used a similar design for the Raichu-

ROP6 sensor. Because the CRIB domain of human PAK1 is known to also interact with plants GTP-bound ROPs (*12*, *38*), we used this domain as a generic probe for ROP6-GTP conformation. Transient expression in *Nicotiana tabacum* leaves confirmed that Raichu-ROP6$^{CA}$ had a higher FRET ratio than Raichu-ROP6. We next analyzed Raichu-ROP6$^{CA\text{-}7Q}$ and found that it has a similar (or even slightly higher) FRET ratio than Raichu-ROP6$^{CA}$. This assay showed that even when the polybasic region in ROP6 C-terminal tail is mutated, ROP6 is still able to interact with a downstream generic effector such as the CRIB domain of PAK. Although it is impossible to test the effect of the 7Q mutations on all the possible effectors of ROP6, this analysis suggests that the 7Q mutations do not impact the overall conformation of ROP6-GTP. Together with the fact that ROP6$^{7Q}$ is still an active GTPase *in vitro* and that the polybasic region is outside of the GTPase domain of ROP6, our analyzes strongly suggest that the 7Q mutations do not impact the folding/conformation of ROP6 and rather specifically affects the interaction between ROP6 and anionic phospholipids.

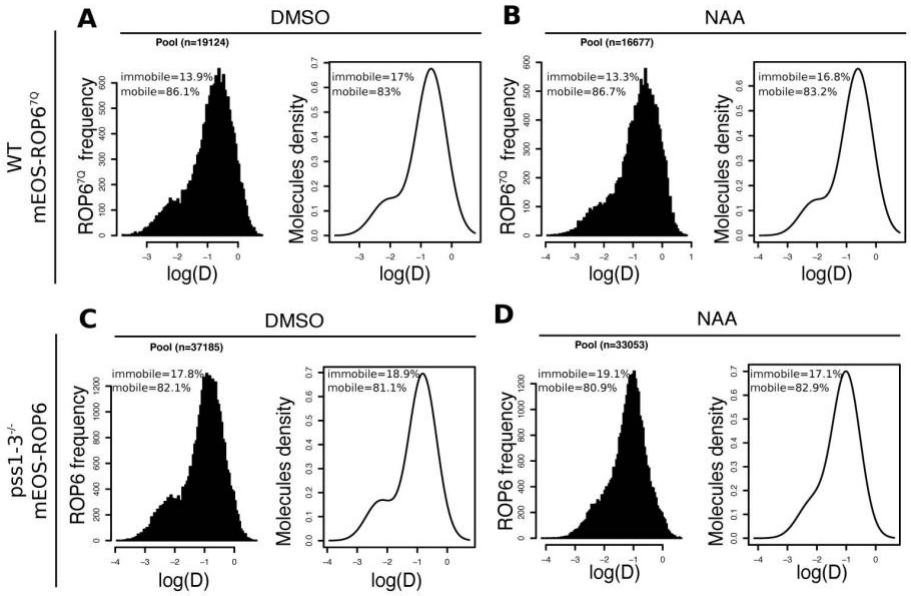


**Fig. S16. Raw data of sptPALM experiments with mEos-ROP6/mEos-ROP6$_{7Q}$ presented in Figure 5. A-D**, Left panel represents the frequency of mEos-ROP6, mEos-ROP6$_{7Q}$ molecules according to their apparent diffusion coefficient (log(D)) obtained by analyzing sptPALM trajectories in mock and auxin-treated condition (NAA, 10µM, 5min) in the wild-type or *pss1-3* mutant background. Right panel represents the distribution of mEos-ROP6, mEos-ROP6$_{7Q}$ molecules according to their apparent diffusion coefficient (log(D)) obtained by analyzing the frequency plot (left panel) using the R mClust package. The percentage of immobile and mobile molecules in each graph represents the percentage of molecules with a trajectory below and above the log(D) of -1.75, respectively. Note that the percentage in left and right panels for each condition are similar (i.e. they vary only from few percent), confirming the existence of two populations with a normal distribution. Note that the right plots in A and B were combined to produce the right plot in Fig. 5F, and the right plots in C and D were combined to produce the left plot in Fig. 5F. "n" corresponds to the number of trajectories analyzed.

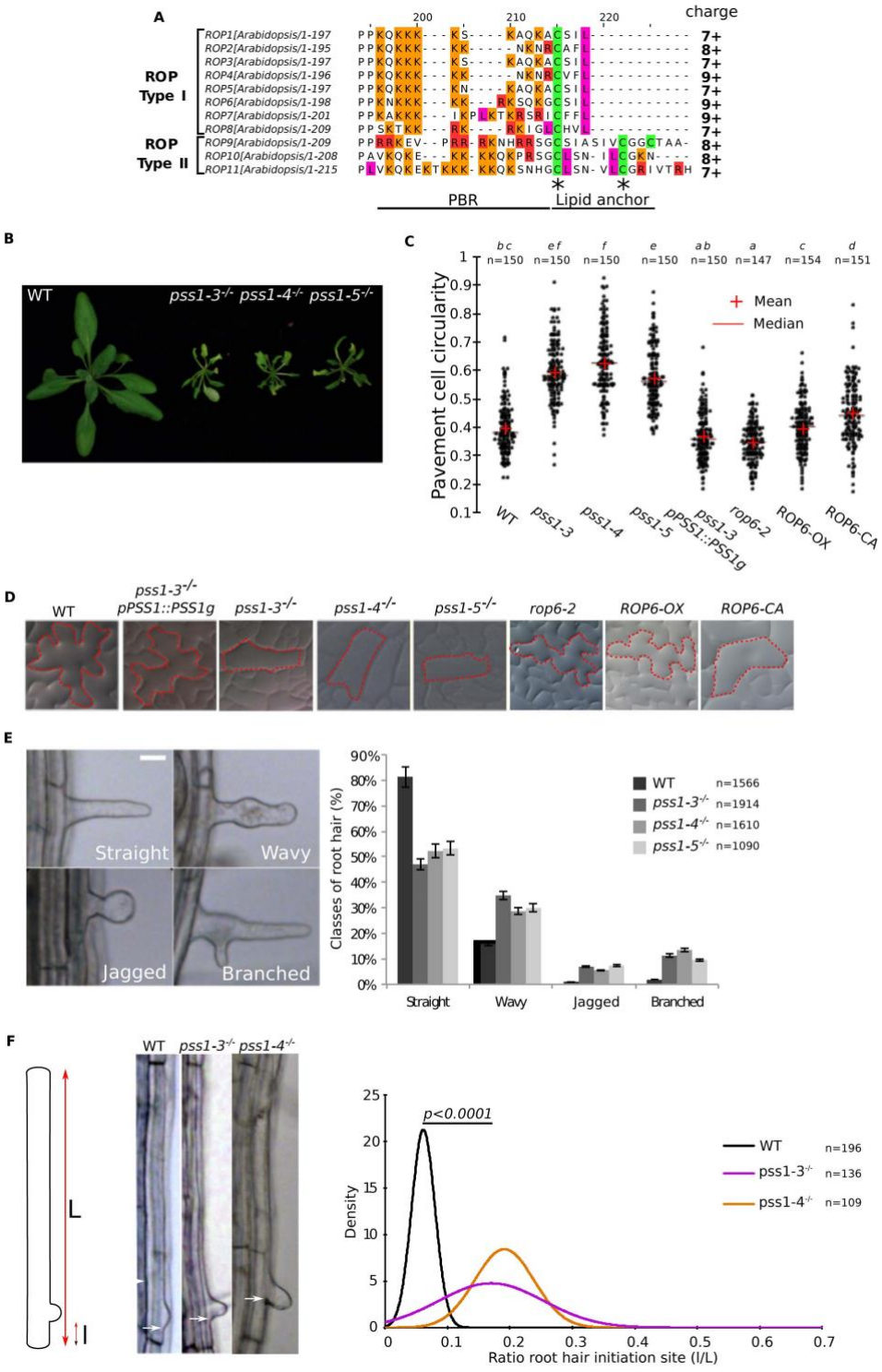


**Fig. S17. PS-less mutants share ROPs-associated phenotypes. A**, Sequence alignment of the C-terminal tail of the 11 Arabidopsis ROPs. Note that they all have a polybasic region with net positive charges ranging from +7 to +9. **B**, Pictures of WT, *pss1-3*$^{-/-}$, *pss1-4*$^{-/-}$ and *pss1-5*$^{-/-}$ rosettes at 21 days after germination (DAG). **C**, Quantification of the pavement cells circularity of WT, *pss1-3*$^{-/-}$, *pss1-4*$^{-/-}$, *pss1-5*$^{-/-}$, *pss1-3*$^{-/-}$x*pPSS1::PSS1g*, *rop6-2*$^{-/-}$, *ROP6-OX (35S::GFP-ROP6)* and

*ROP6-CA (35S::GFP-ROP6$_{CA}$)*. **D**, Picture showing pavement cells shape of WT, *pss1-3*$^{-/-}$, *pss1-4*$^{-/-}$, *pss1-5*$^{-/-}$, *pss1-3*$^{-/-}$x*pPSS1::PSS1g*, *rop6-2*$^{-/-}$, *ROP6-OX* and *ROP6-CA*. **E**, Picture of representative root hair shape phenotypes observed in *pss1* mutants (classified as straight, wavy, bulged and branched), and related quantification. **F**, Representation of root hair initiation site ratio calculation and picture of WT, *pss1-3*$^{-/-}$ and *pss1-4*$^{-/-}$ root hair initiation site, and related quantification. Arrows indicate the root hair initiation site. n represents the number of cells (C), and root hairs (E and F) analyzed, letters indicate statistical differences (see methods for details on statistical tests).

**Movie S1**

Example of video showing mEos-ROP6 single molecule imaging used for sptPALM and livePALM analysis.

**Movie S2**

Video showing GFP-ROP6 localization (10µM NAA, 20 min) in TIRFM before and after bleaching a region of interest containing GFP-ROP6 nanoclusters. Note that GFP-ROP6 nanoclusters are immobile and that they do not recover fluorescence after photobleaching (by contrast to surrounding "non-clustered" GFP-ROP6 signal at the plasma membrane, for which recovery of fluorescence is fast).

**Movie S3**

Video showing GFP-ROP6 localization (10µM NAA, 20 min) in *pss1-3* mutant in TIRFM before and after bleaching a region of interest containing GFP-ROP6 nanoclusters. Note that, like in the WT, GFP-ROP6 nanoclusters are immobile. However, by contrast to the WT, GFP-ROP6 nanoclusters rapidly recover fluorescence after photobleaching.